Optically Coherent Nitrogen-Vacancy Defect Centers in Diamond Nanostructures

Laura Orphal-Kobin,[1] Kilian Unterguggenberger,[1] Tommaso Pregnolato,[1,2] Natalia Kemf,[2] Mathias Matalla,[2] Ralph-Stephan Unger,[2] Ina Ostermay,[2] Gregor Pieplow,[1] and Tim Schröder[1,2,*]

[1]*Department of Physics, Humboldt-Universität zu Berlin, Newtonstraße 15, 12489 Berlin, Germany*
[2]*Ferdinand-Braun-Institut, Gustav-Kirchhoff-Straße 4, 12489 Berlin, Germany*

(Received 20 February 2022; revised 6 February 2023; accepted 7 February 2023; published 20 March 2023)

Optically active solid-state spin defects have the potential to become a versatile resource for quantum information processing applications. Nitrogen-vacancy defect centers (NV) in diamond act as quantum memories and can be interfaced with coherent photons as demonstrated in entanglement protocols. However, particularly in diamond nanostructures, the effect of spectral diffusion leads to optical decoherence hindering entanglement generation. In this work, we present strategies to significantly reduce the electric noise in diamond nanostructures. We demonstrate single NVs in nanopillars exhibiting a lifetime-limited linewidth on a timescale of one second and long-term spectral stability with an inhomogeneous linewidth as low as 150 MHz over three minutes. Excitation power and energy-dependent measurements in combination with nanoscopic Monte Carlo simulations contribute to a better understanding of the impact of bulk and surface defects on the NV's spectral properties. Finally, we propose an entanglement protocol for nanostructure-coupled NVs providing entanglement generation rates up to hundreds of kHz.

DOI: 10.1103/PhysRevX.13.011042

Subject Areas: Condensed Matter Physics, Nanophysics, Quantum Physics

I. INTRODUCTION

Optically active solid-state spin defects are a resource for a variety of quantum applications, including sensing [1], secure communication [2,3], and information processing applications [4,5]. In many proposed quantum repeater protocols, quantum information transfer is achieved by interfacing spin qubits with photons [6–9]. Prominently, the negatively charged nitrogen-vacancy defect center (NV) in diamond has enabled spin-photon and subsequent spin-spin entanglement of distant qubits [10,11], recently even for a three-node quantum network [12]. However, all these impressive experiments have been performed with NVs in bulk samples using solid immersion lenses [13] that are relatively inefficient photonic structures compared to nanostructures [14]. Nanostructures have enabled high photon detection rates [15,16], more efficient fiber coupling [17,18], and increased light-matter interaction [19], and they allow for photonic integration [20]. These improvements are crucial requirements for further quantum technology development, but to date, NVs in any nanostructure have not yet enabled the generation of coherent single-photon states, which are the basis of any entanglement protocol. Lifetime-limited optical transition linewidths for NVs in nanostructures are hindered by the effect of spectral diffusion [21–23]. Defects in the vicinity of the NV act as charge traps and electron donors that can be photoionized, inducing electromagnetic noise and a fluctuating dc Stark shift $U_{\mathrm{Stark}} = -\mathbf{d} \cdot \mathbf{E}(\mathbf{t})$ of the optical transition frequency over time, as illustrated in Fig. 1(a). While in bulklike samples NVs with narrow inhomogeneous optical linewidths below 100 MHz have been demonstrated [24–28], in nanostructures the linewidth is inhomogeneously broadened to hundreds of MHz or even several GHz [20,22,29]. The NV charge environment depends strongly on the material properties and fabrication process, i.e., NV formation, defect density, and diamond structuring methods, as well as the distance from the NV to the surface. In recent works, it was shown that narrow linewidth NVs can be found predominantly for NVs formed from native nitrogen rather than for NVs created by ion implantation, which introduces local lattice damage such as vacancies [25,26]. For shallow NVs, surface defects are considered the main source of charge noise [27]. Although significant efforts have been made over the past decade, the development of micro- and nanofabrication techniques [30,31] and surface termination [32] for improved material quality, as well as active control schemes [33], have not yet been able to sufficiently prevent spectral diffusion in diamond nanostructures.

Here, we investigate the spectral properties of natural, single NVs incorporated in diamond nanostructures with

*tim.schroeder@physik.hu-berlin.de

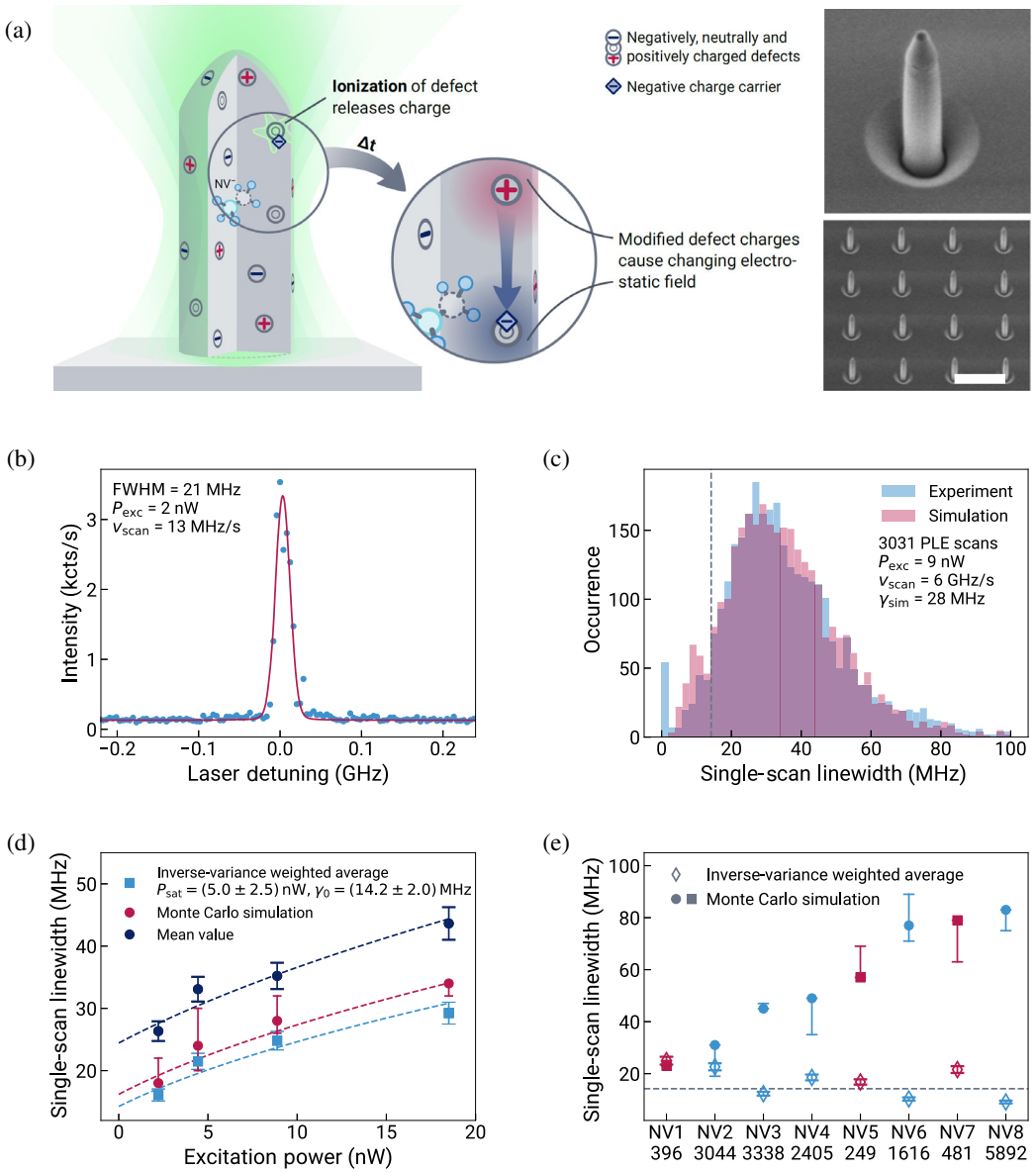

FIG. 1. Nanostructure and single-scan linewidth. (a) Schematic sketch of a NV incorporated in a nanopillar. Green laser irradiation causes ionization of present surface and bulk defects; i.e., charges are released and move within the lattice, for example, to other defects that act as charge traps. This dynamic induces fluctuations of the electrostatic environment of the NV and leads to spectral diffusion of the NV ZPL. Insets: scanning electron microscopy images of a single nanopillar with a radius of 125 nm and a height of 1.6 μm (top) and an array of identical nanopillars (bottom). The scale bar corresponds to a dimension of 2 μm. (b) Single PLE scan described by a Voigt profile. The exemplarily selected spectrum shows a linewidth close to the lifetime limit maintained for about one second. (c) Histogram presenting the occurrence of single-scan linewidth obtained from 3031 PLE scans. The measured data are simulated by a Monte Carlo approach. From the simulations, a power-broadened linewidth of 28 MHz is determined. The gray dashed line indicates the lifetime-limited linewidth of 14 MHz. (d) Single-scan linewidth as a function of excitation power at a scan speed of 6 GHz/s. The single-scan linewidths are evaluated using three methods. The data can be fitted by the function $\gamma = \gamma_0\sqrt{1 + P/P_{sat}}$ describing laser-induced power broadening of the linewidth. For the Monte Carlo simulation, the saturation power and natural linewidth are determined as $P_{sat,MC} = (5.4 \pm 2.2)$ nW and $\gamma_{0,MC} = (16.2 \pm 1.8)$ MHz, and for the mean value approach as $P_{sat,MV} = (8.1 \pm 2.9)$ nW and $\gamma_{0,MV} = (24.4 \pm 2.2)$ MHz. (e) Plot summarizing the single-scan linewidths of eight single NVs in different nanopillars from different sample regions (blue circles and red squares). The NVs are labeled with the number of PLE scans that were taken into account. The excitation power is 19 nW, and the scan speed is 50 GHz/s. In contrast to panel (d), we apply a 525 nm initialization pulse before every line scan. For the linewidth analysis, the Monte Carlo simulation (filled circles and squares) and inverse-variance weighting (empty diamonds) methods are used. The uncertainties of the single-scan linewidths determined by the Monte Carlo simulation are given by the 99% confidence interval. For this fast scan speed, the inverse-variance method is not valid anymore.

radii of 125 nm by performing photoluminescence excitation (PLE) spectroscopy. We systematically examine spectral diffusion in three different excitation regimes: (1) red continuous wave (cw) illumination, (2) two-color excitation with red and higher energetic laser light, and (3) a shutter experiment where the NV is excited after periods of darkness. All three regimes are relevant for prospective quantum applications, for example, entanglement generation. We identify key parameters in control schemes for preserving spectral stability on a timescale of minutes. Furthermore, the comparison of experimental results with nanoscopic Monte Carlo simulations reveals the relation of spectral diffusion dynamics to the type and number of ionized defects. In the presented system, both bulk and surface defects contribute to an overall linewidth broadening. Finally, we propose a control protocol for efficient entanglement generation using NVs coupled to nanostructures based on the findings of this paper.

II. SAMPLE

In contrast to most previous investigations, we select a commercial chemical-vapor-deposition-grown sample with a relatively high density of 1 ppm nitrogen atoms [34] resulting in a density of roughly 10 ppb NV defect centers and a suitable yield in our NV-nanostructure device fabrication of about 10%. Nanopillar fabrication of the ⟨100⟩-oriented single-crystalline diamond substrate was carried out with dry etching processes [35] (Appendix A). The parameters of each step are similar to recipes used in other works but have been adjusted and optimized for the fabrication tools used, minimizing the structural damage of the diamond surface, thus enabling repeatable high-quality fabrication over large areas, as evident in the scanning electron microscopy images in Fig. 1(a). A smooth diamond surface indicates less damage to the crystal structure below the surface. The nanopillar radii of 125 nm are optimized for photon coupling, and the height of 1.6 μm allows for the optical separation of nanopillar NVs from bulk NVs.

III. SINGLE-SCAN LINEWIDTH

The linewidth of the NV zero-phonon line (ZPL) is investigated at temperatures below 4 K by PLE spectroscopy. Here, the frequency of the excitation laser is tuned across the ZPL at 637 nm, and the photons emitted in the phonon-sideband (650–800 nm) are detected. Single-scan linewidths reveal information about the indistinguishability of emitted photons. The data in Fig. 1(b) demonstrate the lifetime-limited linewidth of a single NV embedded in a diamond nanostructure for scan speeds as slow as approximately one natural linewidth per second and for excitation powers of half of the saturation power ($P_{\mathrm{sat}} = 5$ nW, see Appendix C for further details). While this PLE scan is postselected, we also statistically analyze the NV linewidth at different scan speeds and laser powers by performing thousands of PLE scans. Individual linewidths are fitted by a Voigt profile, and the characteristic single-scan linewidth of a data set is determined by using the inverse-variance weighting method and a new evaluation method based on Monte Carlo simulations that we introduce in this work (Appendix C). Because of a low number of detection events per time bin at fast scan speeds resulting in a large relative uncertainty assuming Poissonian statistics, the recorded spectra not only display a large distribution of linewidths but also produce unphysically narrow lines below the lifetime-limited linewidth [Fig. 1(c)]. This discrepancy does not allow for a direct analysis of the linewidth via simple averaging or weighting of the data, a challenge that also applies to previous works. To address this problem, we employ a Monte Carlo simulation: Cauchy-distributed detection events and noise are fitted with a Voigt profile. The resulting linewidths are summarized in a histogram. We then use a χ^2 test to find the best linewidth corresponding to the measured data.

Excitation power-dependent measurements [Fig. 1(d)] allow for finding a parameter regime in which the spectral stability and the negative charge state are preserved for long times while a large number of photons are still emitted. For a scan speed of 6 GHz/s, the effect of power broadening limits the preservation of the lifetime-limited linewidth on average, which is extracted to be (14.2 ± 2.0) MHz for zero excitation power. Comparing standard data analysis methods with our Monte Carlo approach, we find a significant offset for the mean value and only a small deviation by applying the inverse-variance weighting method. However, for faster scan speeds when the number of single-photon detection events is too low to sample the line profile with low relative uncertainty, linewidths determined with both previously used standard methods are prone to non-negligible errors [Fig. 1(e)].

The observed NV properties can be similarly reproduced with NVs in other nanopillars. We investigate two sample regions containing, in total, 180 nanopillars. Of these, about 10% contain single NVs, i.e., appear bright in PL scans. Finally, we measure a PLE signal of eight single NVs in different nanopillars, exhibiting overall narrow linewidths with an extracted single-scan linewidth ranging from close to the lifetime limit to about a sixfold broadening of 83 MHz [Fig. 1(e)]. For this overview measurement, we apply, in contrast to the other measurements, a green re-pump pulse before every line scan to ensure initialization into the negative NV charge state, leading to an additional broadening of the single-scan linewidth compared to Fig. 1(d). All subsequent results presented in this work stem from characterization of NV3.

IV. INHOMOGENEOUS LINEWIDTH AND IONIZATION TIME

Besides single-scan linewidths, which determine photon coherence on short timescales, the inhomogeneous

linewidth of single NVs is an important figure of merit for the performance of quantum entanglement protocols. In this section, we investigate the inhomogeneous linewidth over a timescale of several minutes. After preparing the NV in the negative charge state by using a green initialization pulse, hundreds of consecutive PLE scans are recorded at 2 nW (half of the saturation power) without reinitialization (regime 1). Figure 2(a) shows an example of a range of about 250 PLE scans and the summed PL intensity recorded on a timescale of more than three minutes. The process of spectral diffusion, in which the transition frequency randomly shifts in time, can be clearly seen in the bottom of Fig. 2(a). The sum of intensities of the individual scans constitutes an inhomogeneously broadened linewidth of about 150 MHz, only an 11-fold broadening compared to the natural linewidth [top of Fig. 2(a)]. Although the trajectory presented here is postselected and does not represent the average inhomogeneous linewidth, we demonstrate that under suitable fabrication and control conditions, a remarkably narrow linewidth can be preserved for minutes in diamond nanostructures. In Fig. 2(b), the time evolution of the inhomogeneous linewidth is shown. The full width at half maximum (FWHM) of the inhomogeneous line is determined from a set of trajectories summing the respective intensities for a given time of up to seven minutes, corresponding to 500 consecutive PLE scans. The data include the trajectory shown in Fig. 2(a) (blue circles) as well as the averaged values of equivalent postselected data sets (red triangles), and the results from all measured data sets (dark blue squares). As a postselection criterion, we reject trajectories exhibiting a spectral jump that causes a line-to-line increase of more than 200 MHz of the cumulatively summed inhomogeneous linewidth. In 28% of the measured data, the NV is spectrally stable (< 400 MHz) and remains in its negative charge state for seven minutes while PLE scans are performed. A power law fit indicates that the phenomenon of spectral diffusion induced by resonant laser irradiation is an anomalous diffusion process, more

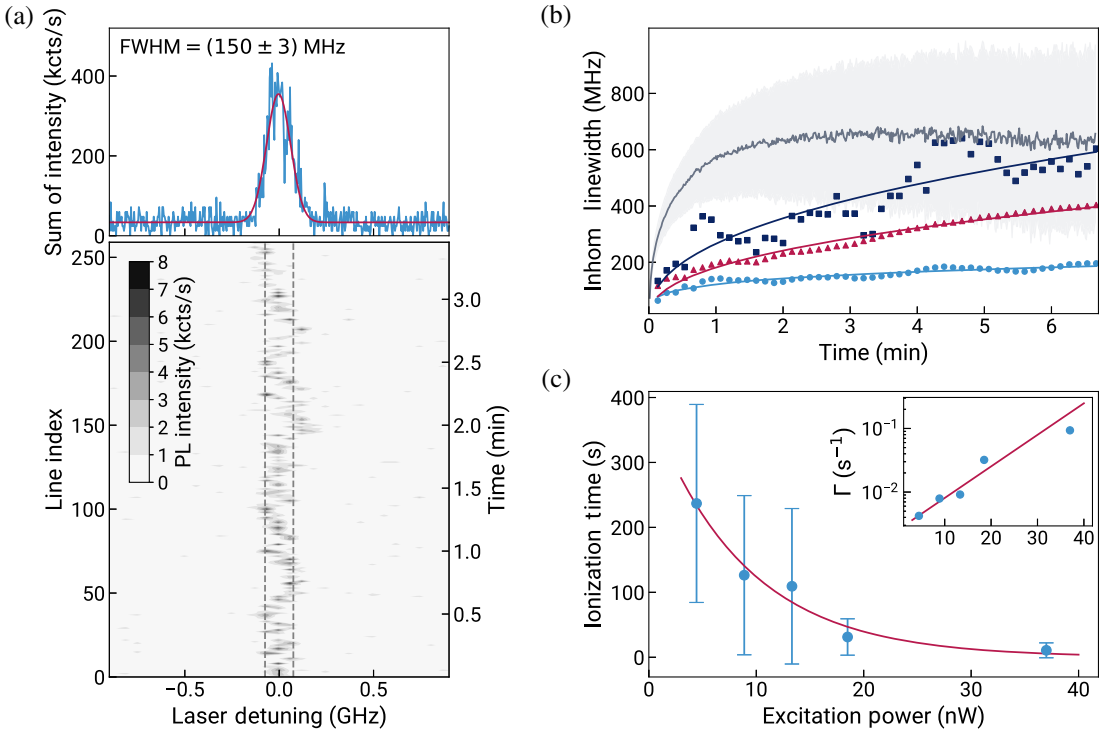

FIG. 2. Inhomogeneous linewidth and ionization time (regime 1). (a) More than 250 PLE scans performed without reinitialization of the NV with green laser pulses. The excitation power of the resonant laser is 2 nW, and the scan speed is 50 GHz/s (bottom). The inhomogeneous linewidth is given by the intensity sum of all scanned lines recorded over a time of more than three minutes and is fitted by a Gaussian function (top). The determined FWHM of (150 ± 3) MHz is indicated by dashed lines (bottom). (b) Cumulative inhomogeneous linewidth evolution in time. Data of the single trajectory corresponding to the PLE scans in (a) ($n = 1$, blue circles), average of postselected trajectories ($n = 14$, red triangles), and all trajectories ($n = 42$, dark blue squares) are shown. The simulated data (gray line) are obtained from modeling a normal diffusion process. The experimental data are fitted by a power law $\gamma_{\mathrm{Inh}} = bP^a$ with exponents $a = 0.22$ (blue line), $a = 0.41$ (red line), and $a = 0.42$ (dark blue line). A scaling exponent $a < 1$ is characteristic for subdiffusive processes. (c) Average ionization time for different excitation powers extracted from many tens of PLE data sets recorded at a scan speed of 12 GHz/s. The uncertainty is given by the standard deviation of the individual ionization times. The ionization time decays exponentially for increased excitation power with a power constant of (8.7 ± 1.4) nW. The NV transition is driven at a duty cycle of about 0.2%. Inset: ionization rate Γ as a function of excitation power.

precisely, a subdiffusive process [36]. Additionally, we use a simple stochastic process (Wiener process, Appendix F) to model the spectral diffusion of the ZPL resonance. We also implement the Ornstein-Uhlenbeck model, but both approaches fail to reproduce the observed evolution of the inhomogeneous linewidth, confirming our conclusion that for the investigated system and chosen excitation parameters, spectral diffusion is likely not characterized by a normal diffusion process.

In addition to spectral diffusion, charge-state stability has been a challenge for NVs in nanostructures [20]. For investigating the ionization time, i.e., the time until the NV converts from the negative to the neutral charge state, we again use a PLE excitation scheme. The NV ZPL transition is driven about 0.2% of the time (duty cycle). The ionization time decays exponentially as a function of excitation power [Fig. 2(c)]. At excitation powers on the order of the saturation power of 5 nW, the ionization time is several minutes. During this time, no green laser pulse needs to be applied for reinitializing the system, resulting in a significantly reduced spectral diffusion, as evaluated in the following section.

V. SPECTRAL DIFFUSION DYNAMICS

Although we have found comparatively long NV ionization times, occasionally the system ionizes. For the charge-state conversion from NV0 to NV-, off-resonant excitation

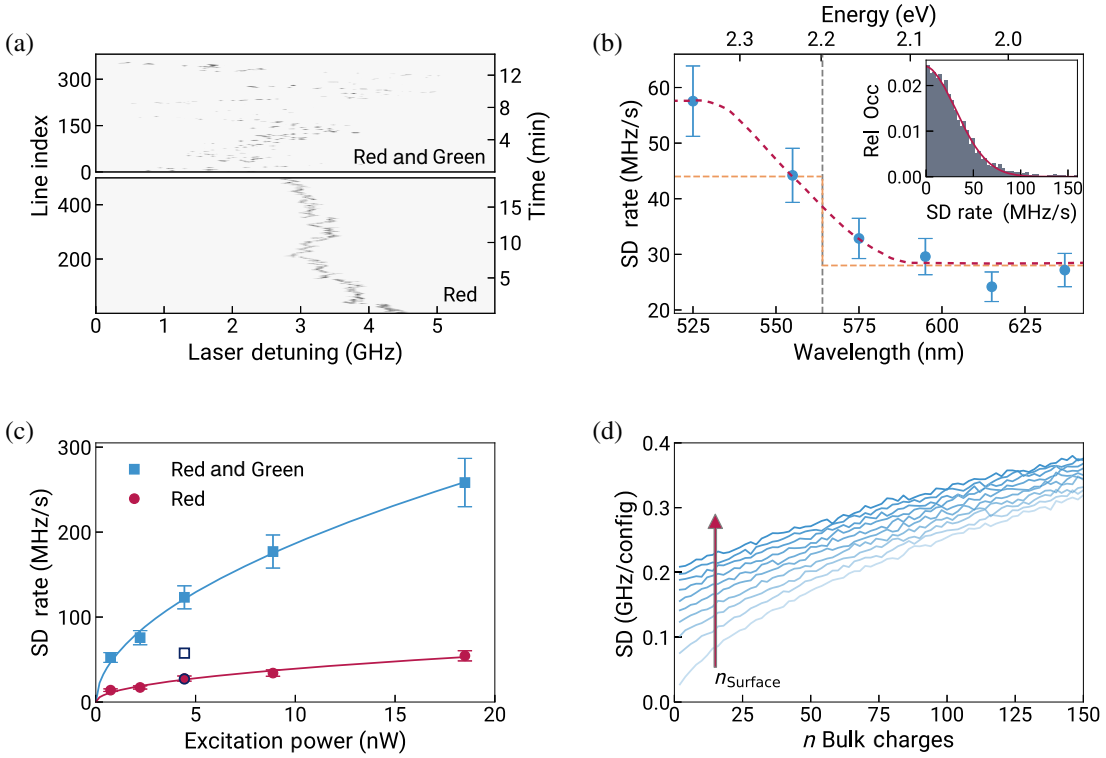

FIG. 3. Spectral diffusion dynamics (regime 2). (a) Hundreds of PLE scans performed with only resonant excitation laser irradiation (bottom) and with a mixture of resonant and green (525 nm) laser irradiation, with an equal ratio of a total power of 4 nW (top). While red laser irradiation induces a small drift of the ZPL resonance frequency, additional green laser light causes large spectral jumps. (b) Spectral diffusion (SD) rate measured for different excitation wavelengths. A two-color PLE scheme, involving resonant and off-resonant laser irradiation, is applied with a total power of 4 nW. The gray dashed line highlights the wavelength of 564 nm, which corresponds to the ionization energy of substitutional nitrogen defects. As a guide for the eye, the supposed spectral diffusion rate evolution is drawn, assuming bulk diamond containing only nitrogen defects (orange dashed line) and additional surface defects (red dashed line). Inset: relative occurrence of spectral shifts described by a normal distribution function. Here, the data excited with a mixture of resonant and 575 nm light are shown. (c) Spectral diffusion rate as a function of the total excitation power, recorded for resonant excitation and two-color excitation with 525 nm light (equal power ratio of on- and off-resonant excitation laser). The spectral diffusion rate scales like a square-root power law with respect to the excitation power: $\Gamma_{SDR} = bP^a$, with exponents $a = 0.49$ for red only and $a = 0.53$ for two-color excitation. The filled markers correspond to data recorded after ten weeks at cryogenic temperatures, and the empty markers to data recorded directly after a warm-up and a second cooldown. (d) Monte Carlo approach with the spectral diffusion of the NV ZPL simulated by placing a certain number of bulk and surface charges at random positions and evaluating the resulting line shift, repeated over many iterations. The number of surface charges is increased from 2 to 452 in the direction of the arrow. Different charge configurations correspond to the fluctuating charge environment during repeated PLE line scans. The increase in spectral diffusion follows an approximate square-root power law by increasing the number of charges.

at 510 to 593 nm [37], as well as energies resonant to the NV0 transition at 575 nm [38], have been used, leading to different reinitialization efficiencies. Compared to 637 nm, the higher laser energies cause ionization of additional diamond impurities and charge dynamics, which in turn lead to increased spectral diffusion, strongly reducing the optical coherence of NV defects [29]. While in PLE scans with only resonant laser light (regime 1, see above) a relatively slow drift of the ZPL resonance over time is observed, two-color excitation using a mixture of resonant and green laser light (regime 2) causes large spectral jumps of the ZPL resonance far exceeding the natural linewidth, as shown in Fig. 3(a). This is not surprising since the sample exhibits a high intrinsic concentration of nitrogen bulk impurities, whose ionization energies are above 637 nm but below 525 nm. Moreover, higher laser energies also enable activation of additional surface defects, inducing further charge noise.

To date, the effect of nonresonant laser irradiation on spectral diffusion of a spectrally stable NV in a nanostructure has not been investigated systematically. We therefore examine energy-dependent spectral diffusion by applying a two-color excitation scheme, using 637 nm in combination with lower wavelength (higher energy) laser light ranging from 525 to 615 nm, and compare it to resonant single-color PLE scans. As a characteristic quantity, we examine the spectral diffusion rate, which is determined as the difference of resonance center frequencies in consecutive line scans normalized by the time step between each scan. In the two-color excitation experiment, we observe a significant increase of the spectral diffusion rate at wavelengths of 555 nm (2.23 eV) and lower [Fig. 3(b)]. Above 555 nm, the relatively low spectral diffusion could be caused by ionization of the relatively few lattice vacancies (GR1, 1.67 eV) [39], defect states based on hydrogen (1.2 eV) [40], or rare boron defects (0.37 eV) [41] in bulk. Below 555 nm, the much stronger spectral diffusion is linked to the ionization of numerous nitrogen C centers (2.20 eV) [40] and a variety of surface defects that are not identified individually (see below).

While energy-dependent measurements reveal the type of defect contributing to spectral diffusion, investigating the excitation power dependence provides insights into the number of defects. We find an approximate square-root power law describing the increase of the spectral diffusion rate as a function of excitation power for both one- and two-color excitation, where the magnitude of the spectral diffusion rate is significantly higher for excitation with additional green laser light [Fig. 3(c)]. This functional relationship is qualitatively confirmed by modeling the impact of a fluctuating charge environment on the NV ZPL resonance with a Monte Carlo simulation [Fig. 3(d), Appendix G]. For the simulation, the NV is placed in the center of a cylindrical volume with the same dimensions as the investigated nanopillars, and it is surrounded by randomly distributed charge traps at a density of 1 ppm according to the density of the C centers. In many iterations, a fixed number of positive and negative charges are randomly distributed among the charge traps, representing the change of the charge environment during repeated line scans. A comparison of experiment and simulations indicates that there is a direct correlation between laser power and number of charges participating in the process.

Further insights into the contribution of bulk and surface defects are gained by comparing the sample after ten weeks at cryogenic temperatures and directly after a warm-up and a second cooldown. Remarkably, the overall excellent spectral properties of the investigated NV were preserved. Moreover, a comparison of the spectral diffusion rates produced by the two-color excitation at 525 nm with a power of 4 nW before the second cooldown with the corresponding values after the second cooldown reveals a significant reduction, whereas the spectral diffusion rate for resonant excitation remains similar [Fig. 3(c)]. Although changes of the defect formation in the bulk crystal are possible, we suppose it is far more likely that the warm-up led to a release of nonubiquitous surface defects, e.g., a layer of ice that had built up over time. Our simulations support this idea: For low excitation powers, the number of participating bulk charges is relatively small. The impact of surface charges in this regime is much more pronounced and can cause a manyfold increase of the spectral diffusion rate, as shown in Fig. 3(d).

VI. NV IN THE DARK

In previously demonstrated entanglement protocols, NVs were not exposed to laser light permanently, but resonant single-shot excitation pulses of the ZPL transitions were applied. To investigate the influence of spectral diffusion in nanostructures during darkness (regime 3), we perform a shutter experiment. Here, the defect is exposed to resonance-scanning laser irradiation of 2 nW for 20 seconds and kept in darkness for 60 seconds in alternation without using green repump pulses [Fig. 4(a), Appendix B]. The frequency difference of the ZPL resonances before and after darkness (which would correspond to the difference of two single-shot readout events) is, on average, 40 MHz, and the main occurrence is about 10 MHz, as summarized in the histogram in Fig. 4(b). This measurement shows that without laser irradiation, spectral diffusion is strongly reduced.

VII. TOWARDS ENTANGLEMENT PROTOCOLS

All previous long-distance spin-spin entanglement experiments based on defect centers in diamond [10–12] were demonstrated with NVs embedded in solid immersion lenses, which are bulklike microstructures that maintain optical coherence but provide limited NV-to-fiber coupling efficiencies. Entanglement attempt rates as large as

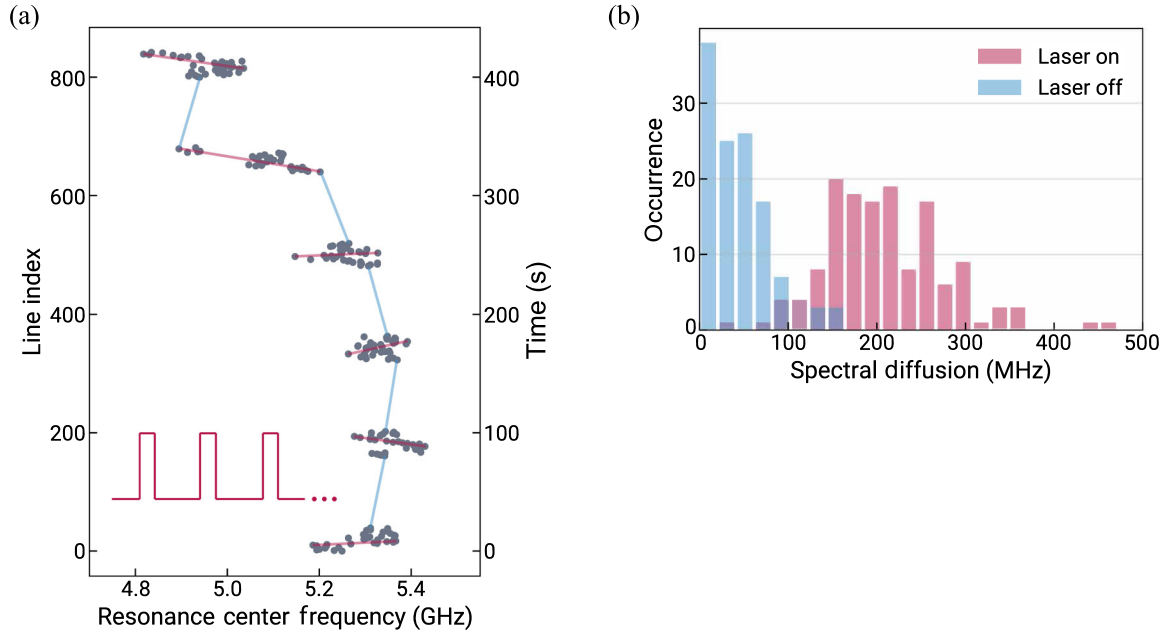

FIG. 4. NV in the dark (regime 3). (a) Shutter experiment in which we alternate between PLE scanning for 20 s and blocking the radiation for 60 s. When PLE scans are performed, the center frequency of the ZPL resonance is extracted from Voigt fits (gray dots). Here, a data set is exemplarily presented. (b) Occurrence of spectral shifts obtained from many data sets. The extracted spectral diffusion value for "Laser on" corresponds to the spanned frequency range recorded in a period of 20 s. The spectral diffusion for "Laser off" is extracted from the spectral difference of the last PLE scan before and the first scan after blocking the laser, as illustrated in panel (a).

182 kHz and successful deterministic entanglement delivery at 10 Hz were demonstrated [11]. Nanostructures could potentially enhance the performance: Improved design parameters enable enhanced photon collection efficiencies [16–18], and increased light-matter interaction in the form of Purcell enhancement can be achieved [19,22,42,43]. Considering the findings of our work, it might be possible to apply nanostructure-embedded NVs for the generation of entanglement. To quantify the potential advantage, we adapt the established entanglement protocols based on π-pulse excitation to the specific requirements of our NV-nanostructure system. In particular, we analyze the protocol with respect to the three investigated excitation regimes that represent the different laser control regimes in entanglement generation, namely, (1) resonant excitation, (2) higher energetic laser irradiation for initialization, and (3) dark diffusion.

We determine resonant π-pulse parameters for the investigated NV of a duration of 2 ns and a peak power of 3 μW, which is technically easy to achieve (see Appendix D for further details). From the spectral diffusion power-law fit [Fig. 3(c)], we extract a spectral diffusion rate of 640 MHz/s during excitation pulses and use this value as an input parameter in a simple stochastic model of the spectral diffusion process to evaluate the coherence of the emitted photons (Appendix E). We assume that the inhomogeneous linewidth σ_{ih} is bounded by the diffusion law $\sigma_{\mathrm{ih}} \propto \Gamma_{\mathrm{SDR}}\sqrt{t}$, where Γ_{SDR} is the spectral diffusion rate and t the evolution time. Based on this diffusion law, we derive the number of entanglement attempts, i.e., π-pulse excitations, that can be applied until the line is broadened by a certain amount. For example, an inhomogeneous broadening of 1% is a relevant regime as it still enables a Hong-Ou-Mandel visibility of around 90% and an entanglement fidelity for creating a photonic Bell state with an optical circuit of up to 87%, which we extract from Ref. [44].

Independent of the type of nanostructure, the NV's spectral properties are assumed to be similar as presented in this work when the NV is located with at least a 125 nm distance to the surface. Considering an optical nanocavity, Purcell enhancement leads to a lifetime reduction and, consequently, to a broadening of the homogeneous linewidth [19]. According to our stochastic model, for a fixed spectral diffusion rate, a broadening of the homogeneous linewidth allows for more entanglement attempts that can be applied while optical coherence is maintained [Fig. 5(b)]. Assuming a threefold broadening of the natural linewidth, we expect to make 222 entanglement attempts until the total linewidth is broadened by 1%. Based on this result, we propose a control protocol for NVs in different types of nanostructures, taking into account the average time it takes for steady spectral realignment as well as system preparation after reinitialization based on PLE scans and Stark tuning [45] [Fig. 5(a), Appendix E]. Entanglement attempt rates ranging from 4 kHz up to 370 kHz can be achieved, considering the present system with a Purcell factor set to one and other types of nanostructures that provide larger Purcell enhancement

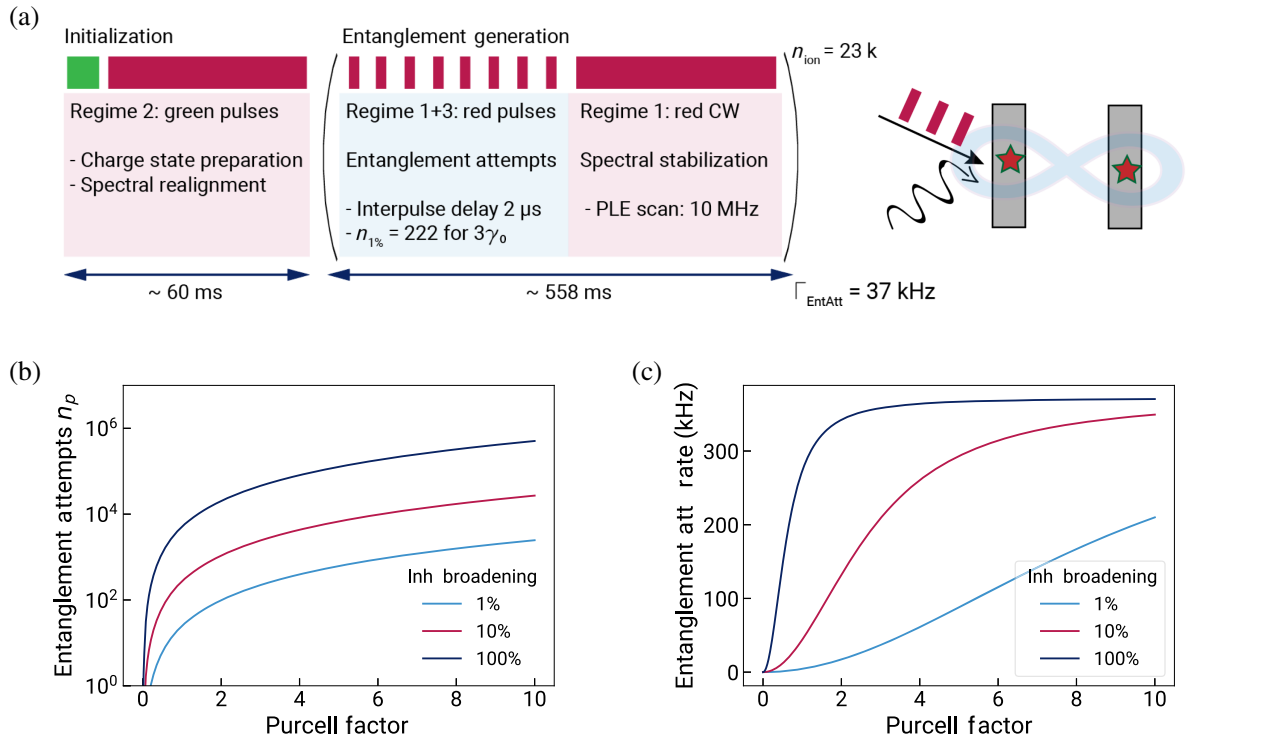

FIG. 5. Towards entanglement generation. (a) Entanglement protocol consisting of periods of system preparation (red) and entanglement generation (blue), with different periods assigned to the three excitation regimes discussed in this work. Here, we assume a threefold Purcell enhancement of the ZPL emission, and the protocol is bounded to the condition that only entanglement attempts (including optical spin-repump pulses) can be applied until the inhomogeneous linewidth is broadened by 1%. Then, a spectral stabilization protocol needs to be applied to tune the resonance back to the target frequency (5 ms). When the NV ionizes, the system is initialized by applying a green laser pulse. The protocol sequence for NV preparation involves charge-state initialization as well as spectral realignment. Inset: illustration of entanglement generation of two distant NV spin qubits embedded in nanostructures by applying coherent laser pulses (red) and microwave pulses (wavy line). (b) Entanglement attempts (number of π pulses) that can be applied until the total linewidth broadens by p percent due to spectral diffusion at a rate of 640 MHz/s as a function of Purcell enhancement, which can be engineered in different types of nanostructures. The estimated natural linewidth of $\gamma_0 = 14.2 \pm 2.0$ MHz considered in the model is increased by the corresponding Purcell factor. We model the inhomogeneous broadening of the linewidth with a Wiener process. Here, an inhomogeneous linewidth broadening of 100% corresponds to a broadening of twice the homogeneous linewidth. (c) Entanglement attempt rate using the protocol depicted in panel (a) as a function of the Purcell factor. For large Purcell factors, the entanglement attempt rate approaches a value of 370 kHz, which is given by the π-pulse separation of 2 μs, the estimated ionization time, and the initialization time.

[Fig. 5(c)]. Here, the maximum entanglement rate is limited by the entanglement attempt duration of 2 μs adapted from Ref. [11] and system preparation time after ionization, which could both be technically improved.

Besides reducing the sensitivity to spectral diffusion, resonant nanostructures can significantly increase the successful entanglement delivery rate by optimized fiber coupling. In previous work, a coupling of 54% of NV emission into a cavity mode was demonstrated, together with a 2.7-fold Purcell enhancement [19]. It was also shown that diamond cavity photons can be fiber coupled and detected with an overall system efficiency of 85% [46]. Combining these achievements, we expect that, for a cavity-coupled NV, 46% of all photons are emitted into the ZPL and fiber coupled for entanglement generation. An enhancement in ZPL emission and photon collection efficiency by more than 2 orders of magnitude would enable appropriate entanglement delivery rates up to hundreds of kHz.

VIII. CONCLUSION

In this article, we demonstrated spectrally stable NVs in diamond nanostructures enabled by a combination of methods ranging from selection of material properties and suitable fabrication recipes to specific control schemes. The choice of a substrate providing natural NVs and the careful adaption of established fabrication methods facilitate reduced structural damage. In addition, the high density of 1 ppm of substitutional N possibly introduces a screening volume between the NV and the bulk, as well as surface charge traps when only a low-energy resonant laser is applied. However, additional systematic investigations are required to quantify the influence of the N density on

spectral diffusion rates and to fully reveal the mechanisms that lead to the observed, reduced diffusion in nanostructures. Under high-energy green laser irradiation, the substitutional N, however, is ionized, leading to strong charge dynamics inducing fast spectral diffusion. We therefore implemented sample-specific control sequences, i.e., maximizing sequences of weak resonant excitation and reducing high-energy initialization pulses. Increasing resonant control sequences is enabled by sample-specific properties, such as long ionization times. Not applying high-energy reinitialization pulses and possible screening of surface charge dynamics significantly reduces charge noise compared to previous works of NVs in nanostructures. Finally, a narrow inhomogeneous linewidth of the NV ZPL over minutes was demonstrated.

The overall spectral stability was confirmed by recording a large number of trajectories, ensuring statistical significance of our findings. While one defect was investigated in detail, we identified seven other color centers with narrow single-scan linewidths. We performed a systematic characterization of the spectral diffusion of the NV ZPL resonance under different excitation regimes and investigated the contribution of bulk and surface defects by complementing the experimental results with a nanoscopic model. We suppose that our methods are applicable to any other nanostructure with natural NVs located about 125 nm from the surface. Therefore, a proposal of distributed NV-NV entanglement generation is presented, which can, taking advantage of increased photon collection efficiencies and Purcell enhancement in nanocavities, prospectively yield increased entanglement rates up to hundreds of kHz. In conclusion, we demonstrated a device based on a nanostructure-coupled NV with optical properties suitable for quantum coherent control protocols.

The data that support the findings of this study are available from the corresponding author upon reasonable request. The most relevant code for data analysis and simulations can be freely accessed at [47].

ACKNOWLEDGMENTS

The authors would like to thank J. H. D. Munns, H. Bernien, and O. Krüger for helpful discussions and, moreover, J. H. D. M. for technical support in the early stages of building the setup. L. O.-K. was supported by the state of Berlin through the Elsa-Neumann scholarship. Moreover, we acknowledge funding by the Federal Ministry of Education and Research (BMBF, Project "DiNOQuant" No. 13N14921, Project QR.X with Subproject No. KIS6QK4001, Project QPIS No. 16KISQ032K) and the European Research Council (ERC Starting Grant "QUREP").

The confocal-microscopy setup was constructed by L. O.-K., and project-specific extensions were added together with K. U. L. O.-K. carried out the PLE measurements. Programs for data analysis were developed by K. U. based on preliminary programs by L. O.-K. G. P. developed and implemented the Monte Carlo linewidth simulation, the stochastic diffusion model, and the Monte Carlo simulation of the fluctuating electric field. The entanglement protocol proposal was worked out by L. O.-K., G. P., and T. S. The diamond nanostructure sample was fabricated at the Ferdinand-Braun-Institute. Here, N. K. and T. P. were responsible for the diamond process, M. M. performed the electron lithography, I. O. the SiN mask deposition, and R.-S. U. the dry etching process. T. S. developed the idea and supervised the project. All authors contributed to the writing of the manuscript.

APPENDIX A: SAMPLE PREPARATION

The nanostructures were fabricated on a commercially available ⟨100⟩-oriented single-crystalline diamond substrate, grown by chemical vapor deposition [34]. The sample surface was initially cleaned in a boiling tri-acid solution (1∶1∶1 of H_2SO_4: HNO_3: $HClO_4$) [48] and subsequently etched in Cl_2- and O_2-based plasmas in order to remove any organic contaminants and structural defects [49]. The fabrication process of the nanopillars is schematically outlined in Fig. 6 and similar to those presented in previous works [35]. After the deposition of a 200 nm-thick layer of Si_3N_4 in an inductively coupled-plasma (ICP) enhanced CVD system, the sample is spin coated with 300 nm of electro-sensitive resist (ZEP520A) and patterned by e-beam lithography. After development, the pattern is transferred into the Si_3N_4 layer by a reactive ion etching process in a CF_4-based plasma (10 sccm, rf power = 100 W, $P = 1$ Pa) and subsequently etched into the diamond during an ICP process (O_2, 80 sccm, ICP power = 750 W, rf power = 200 W, $P = 0.3$ Pa). We use pure O_2 plasma and not a mixture of O_2 and Ar as some groups report, which may have resulted in a reduced level of damage on the exposed diamond surface. Ar is mainly used to enhance the sputtering effect during the plasma process, usually to improve etch rate and verticality. This process, however, is quite "physical" and energetic, as it is based on the fact that the Ar particles in the plasma are accelerated towards the exposed surfaces of the diamond and remove the material by sputtering away the C atoms. The sample is finally cleaned in a buffered-HF solution, which completely dissolves the Si_3N_4 layer and thus exposes the diamond surface.

A scanning electron microscopy (SEM) image of a section of the nanopillar array is shown in Fig. 1(a). The nanopillars investigated in this work have a diameter of approximately 250 nm and a height of 1.6 μm, as estimated from SEM images.

We investigated two sample regions containing 180 nanopillars. Of these, about 10% contained at least a single NV, i.e., appeared bright in PL scans. In 44% of these nanopillars, we were able to measure a PLE signal. No effort was put into understanding why PLE measurements

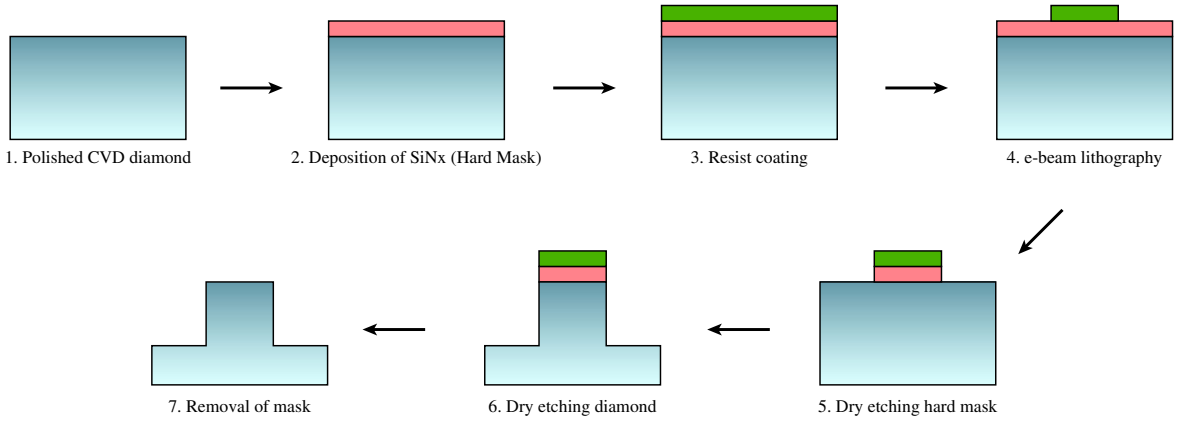

FIG. 6. Fabrication steps. Dry-etching fabrication process of diamond nanostructures.

were not successful in the remaining 56%, but it could be due to fast ionization rates or long T1 times after spin mixing, as no repump signal was applied.

APPENDIX B: EXPERIMENTAL DETAILS

1. Setup

The nanostructures are investigated in a home-built confocal microscopy setup at cryogenic temperatures at about 3.8 K by using a closed-cycle helium cryostat (AttoDRY800). The signal photons are collected by using an objective with a numerical aperture of 0.82 and coupling the signal into a single-mode fiber. For resonant excitation, a tunable diode laser (New Focus Velocity TLB-6704) is used, which is scanned by applying an external piezo voltage. Energy-dependent measurements are performed by applying a SuperK FIANIUM FIU-15 laser system with a bandwidth of 10 nm and a repetition rate of 78 MHz. For the wavelength readout, a wavelength meter (HighFinesse WS/7) at an integration time of 2 ms is used. Single photons are detected by two avalanche photodiodes of the series SPCM-AQRH by Excelitas Technologies. For controlling and synchronizing all devices involved in the experiment, a control software based on QuDi [50]—a modular laboratory experiment management suite—is used. All devices were interfaced with the PYTHON-based software suite, and already-existing modules were adapted for our purposes. As a hardware interface, the USB-6343 Multifunction I/O Device from National Instruments is used. In this work, no microwave driving or optical spin-state manipulation such as resonant excitation of the $m_s = \pm 1$ transitions is applied.

In PLE scans, we recorded single-scan linewidths while the laser was scanned back and forth. The duration of a single scan is given by the scan speed and scan range, which was, in most experiments, about 6 GHz. Between a back and forth scan, there is a break of approximately 150 ms. To limit an error due to laser piezo hysteresis, we only considered data that were recorded when the laser was scanned in one direction for analysis of the inhomogeneous linewidth. In this work, the laser frequency scan speed ranged from as low as 13 MHz/s up to 50 GHz/s depending on the purpose of the measurement. A high scan speed, for example, is beneficial for finding bright and stable NVs. However, we noticed that, for our sample, the optimal scan speed for detailed linewidth characterization was 6 GHz/s. Too-fast scan speeds can lead to undersampling of individual PLE scans, and in this case, reliable results cannot be extracted by using standard methods such as inverse-variance weighting.

In all measurements, except the data presented in Fig. 1(e), the NV was only initialized by a green repump pulse, when it was ionized after performing many individual PLE scans.

2. Shutter experiment

The laser was switched on and off by using a mechanical shutter while PLE scans were performed continuously. Since even weak laser irradiation during the PLE scans (a few hundred ms) induces spectral diffusion, we argued that for a π-pulsed single-shot excitation on the nanosecond timescale, spectral diffusion would be much more suppressed, if not fully absent.

3. Two cooldowns

The experiments were performed on a timescale of 12 weeks in total. After ten weeks, we warmed up the system to room temperature and subsequently cooled it down again to continue measurements for another two weeks. We were able to find exactly the same defect NV3 that we used for detailed investigations discussed in the main text. In the first cooldown, we recorded the data presented in Figs. 1(b)–1(e) (red and NV3), 2, 3(a) and 3(c), as well as the shutter experiment shown in Fig. 4. In the second run, the data presented in Figs. 3(b) and 1(e) (blue) were recorded. By comparing the excitation power-dependent spectral diffusion rate and single scan linewidth

at resonant excitation power, the preservation of the overall good optical properties could be confirmed. However, for two-color excitation schemes with additional green laser light, we notice a significant difference in the spectral diffusion rate. As discussed in the main text, we assume that after a long time at cryogenic temperatures, a layer of ice builds up on the surface, as was also already suggested in previous works. Warming and again cooling down the system led to a release of the nonubiquitous surface defects. Although possible, we assume that a change of the defect configuration inside the pillar is unlikely.

APPENDIX C: DATA ANALYSIS

The raw PLE data are binned to a resolution of 4 MHz. To ensure that only PLE scans providing sufficient signal photons are taken into account in the analysis, we only consider scans where at least one bin contains at least three photons.

The single-scan line profile is described by a Voigt profile that is the convolution of a Gaussian and a Lorentzian distribution function. We use a least-squares minimization algorithm for fitting, in the implementation provided by the lmfit PYTHON package [51]. The Voigt distribution function is modeled by

$$f(x;A,\mu,\sigma,\gamma)=\frac{A\mathrm{Re}[w(z)]}{\sigma\sqrt{2\pi}}, \tag{C1}$$

where

$$z=\frac{x-\mu+i\gamma}{\sigma\sqrt{2}} \tag{C2}$$

and

$$w(z)=e^{-z^2}\mathrm{erfc}(-iz). \tag{C3}$$

Here, A is the amplitude, σ corresponds to the characteristic width, and μ is the center. The FWHM is approximated by 3.6013σ. The characteristic single-scan linewidth of a data set is determined by the inverse-variance weighted average [52], if the Monte Carlo method for fast scan speeds is not used (see below). The spectral diffusion rate is obtained by calculating the difference between extracted resonance center frequencies of consecutive line scans, computing the inverse-variance weighted average, and dividing it by the time between scans.

1. Error estimation and data processing

The relative measurement uncertainties due to slight alignment inaccuracies is 5% for the single-scan linewidth (FWHM) and 11% for the spectral diffusion rate. These values are estimated by comparing similar measurements that were performed on different days. Since the wave meter is read out only at the beginning and end of each scan, nonlinearities due to piezo hysteresis are unaccounted for. By comparison with continuous readout, we can quantify its contribution to the relative error budget to be 6%. The finite precision of the wave meter contributes 2%. Both error sources are intrinsically reflected in the overall relative measurement uncertainty.

2. Monte Carlo linewidth simulation

Fast spectral scans, for example at scan speeds of 50 GHz/s, make it difficult to determine the homogeneous linewidth of an emitter because only a few photons are collected in a single scan. Our statistical analysis shows that fitting single-line scans with a Voigt profile, which involve fewer than 20 photons, will skew the main occurrence of linewidths towards unphysically narrow lines. To ameliorate this problem, we elect to use a Monte Carlo simulation of the line scan and fitting procedure, allowing us to better determine the homogeneous linewidth of spectrally unstable emitters. A single iteration of the simulation contains the following steps: A number of detection events are drawn from a Poisson distribution with a fixed mean. The events are scattered along a fixed frequency interval, weighted by a Cauchy distribution with a fixed width γ. The resulting spectrum is then fitted with a Voigt profile, and the resulting FWHM and fitting error is recorded. This is repeated for at least as many iterations as there are line scans in the experiment. We reject lines, if no frequency bin (4 MHz width) with at least three photon counts is present. Crucially, the Monte Carlo simulation allows for a change in the mean number of photon detection events (N) and the linewidth of the Cauchy distribution. The linewidth statistics of the Monte Carlo simulation can then be used to determine both parameters, linewidth and average photon number, by comparing them with the experimental data. As in Ref. [53], we use a χ^2 test to determine a best estimate of the parameters:

$$S(\gamma,N)=\sum_{i=0}^{N}\frac{[O_i-E_i(\gamma,N)]^2}{E_i(\gamma,N)}, \tag{C4}$$

where O_i are the occurrences of the observed linewidths in a spectral bin labeled by i and $E_i(\gamma,N)$ are occurrences of the simulated linewidths in the same spectral bin. By minimizing $S(\gamma,N)$, we can determine the γ and N that best fit the observed data. Even though the simulations qualitatively reproduce a large occurrence of unphysically narrow lines, they still do not match the observed data perfectly. Smaller linewidths $\gamma\leq 15$ MHz are therefore counted in a single bin. The binning for larger linewidths has to be adjusted according to both the observed and simulated data because frequency bins with fewer than 5 counts on average will make the fitting procedure more unreliable. The details of the procedure can be found in

Ref. [53]. The 99% confidence interval for γ can be found by determining the γ and N for which

$$S(\gamma, N) \leq S(\gamma_{\min}, N_{\min}) + 9.21. \tag{C5}$$

The results for a range of pillars for 50 GHz/s scan speeds and an excitation power of 19 nW can be seen in Fig. 1(e) and for a scan speed of 6 GHz/s in Figs. 1(c) and 1(d).

3. Saturation power and power broadening

The saturation power of a two-level system is a characteristic parameter that, for example, will be used later to determine π-pulse parameters. We examine two methods to extract the saturation power of NV3. First, in an excitation power-dependent PLE measurement, the mean peak count rate is evaluated [Fig. 7, same data set as used for Fig. 1(d)]. The detected intensity I can be described as a function of the incident laser power P,

$$I = I_{\text{sat}} \frac{P}{P + P_{\text{sat}}}, \tag{C6}$$

where P_{sat} is the saturation power and I_{sat} is the corresponding count rate. Before the fit is performed, we subtract the background from the signal data. From the saturation curve fit, we determine a saturation power of $P_{\text{sat}} = (5.1 \pm 1.4)$ nW and a saturation intensity of $I_{\text{sat}} = (30 \pm 3)$ kcts/s.

Second, we investigate the broadening of the ZPL linewidth as a function of the PLE laser power. In an ideal two-level system—for example, an isolated atom—the absorption linewidth broadens with excitation power [54],

$$\gamma = \gamma_0 \sqrt{1 + \frac{P}{P_{\text{sat}}}}. \tag{C7}$$

Here, γ corresponds to the broadened linewidth and γ_0 to the natural linewidth at zero laser power. The expression in Eq. (C7) is used for fitting the data presented in Fig. 1(d). From the power-broadening fit, we obtain a saturation power $P_{\text{sat}} = (5.0 \pm 2.5)$ nW and a natural linewidth of $\gamma_0 = (14.2 \pm 2.0)$ MHz at zero laser power. The values we obtain for the saturation powers by applying the two different methods are in very good agreement with each other. While the obtained value for the natural linewidth indicates a Purcell enhancement in comparison to the expected bulk value of 12 MHz, in previous work, for comparable nanostructures, a NV lifetime of (14.6 ± 1.9) ns was observed, leading to a natural linewidth ranging from 9.6 to 12.5 MHz [35]. However, even though the compared structures are not identical and the position of the NVs within the nanopillars is not known, the natural linewidths are overlapping within the given uncertainties.

To prove that the linewidths obtained from single-line scans are predominantly homogeneously broadened and the description of the broadening with Eq. (C7) is valid, we evaluate the spectral diffusion rate. Considering a scan speed of 5.88 GHz/s and an average single scan linewidth of 29 MHz at 19 nW excitation power [compare with Fig. 1(d)] leads to an average time of 4.9 ms where the excitation laser is on resonance. The corresponding spectral diffusion rate is 49 MHz/s. Finally, during the time of 4.9 ms that we probe the resonance with the excitation laser, the induced spectral diffusion is estimated to be 0.24 MHz, approximately 1% of the recorded average linewidth, and thus negligible.

APPENDIX D: TOWARDS ENTANGLEMENT GENERATION

In previous works, NVs in solid-immersion lenses were used for demonstrating remote entanglement based on resonant single-shot excitation of the ZPL transitions

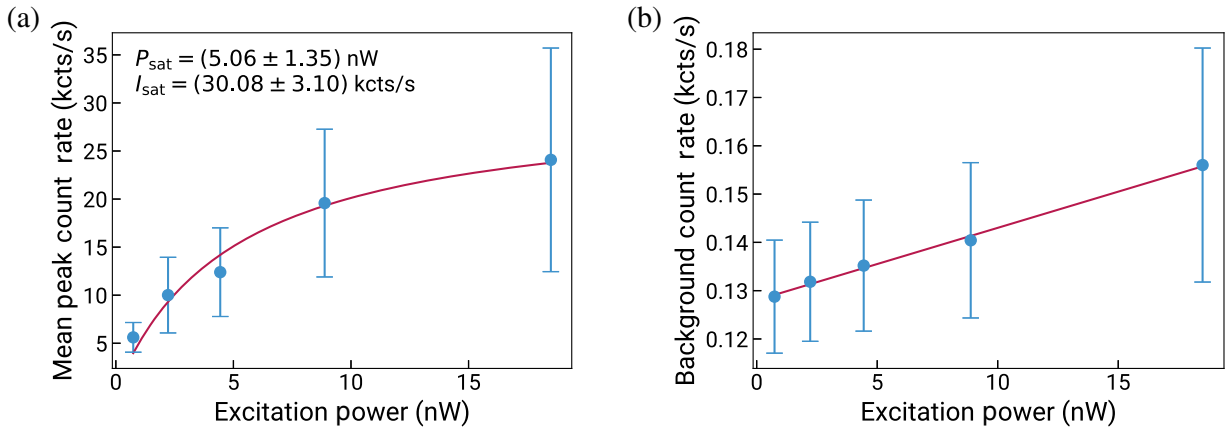

FIG. 7. Saturation measurement. (a) Mean peak count rate as a function of the resonant excitation power (scan speed 6 GHz/s) extracted from the excitation power-dependent PLE measurements. The error bars are given by the standard deviations. The fit function is from Eq. (C6). The background at the corresponding excitation power was already subtracted. (b) Background count rate increasing linearly with excitation power. The intercept at zero excitation power is at 128 cts/s.

through π pulses [10,11]. There, in optimized protocols, an entanglement attempt duration of 5.5 μs is demonstrated, corresponding to a rate of 182 kHz, whereas a duration of less than 2 μs (>500 kHz) is proposed for minor modifications of the classical experimental control protocol. As a final result, a rate of 10 Hz for successful deterministic entanglement delivery was achieved. Regarding successful entanglement generation using NVs in nanostructures, we propose that for optimized protocols and system efficiencies, the lower spectral stability in comparison to NVs in solid-immersion lenses can be compensated. For NVs coupled to nanostructures—for example, optical nanocavities—we expect higher emission into the ZPL and increased photon collection efficiencies, resulting in an overall increased rate of entanglement generation by orders of magnitude.

In the main text, we derive an entanglement protocol and a figure of merit for entanglement generation in diamond nanostructures, taking our findings on spectral diffusion dynamics into account. From experimental results, central quantities such as π-pulse parameters and ionization time are estimated.

1. π-pulse parameters

From the steady-state solution of the optical Bloch equations, we derive

$$\frac{P}{P_{\mathrm{sat}}} = \frac{2\Omega^2}{\gamma_0^2}. \tag{D1}$$

Here, Ω is the Rabi frequency of the two-level system. We determine the power needed to perform a π-pulse rotation, an electric field pulse driving the ZPL transition with $\Omega T_\pi = \pi$, depending on the emitter lifetime τ_1, the pulse duration T_π, and the saturation power P_{sat}:

$$P_\pi = 2\left(\pi\frac{\tau_l}{T_\pi}\right)^2 P_{\mathrm{sat}}. \tag{D2}$$

For the investigated NV from the homogeneous linewidth, we estimate a lifetime of $\tau_1 = 11.2$ ns and use the saturation power of $P_{\mathrm{sat}} = 5.0$ nW as parameters for a rectangular π pulse with $T_\pi = 2$ ns pulse duration and a corresponding power of $P_\pi = 3.1$ μW.

2. Spin-repump pulses

In previous work, additional optical spin-repump pulses were applied before every entanglement attempt [10,11]. In the presented sample, there is no clear evidence for a significant impact of spin mixing. When spin mixing occurs with high probability, dark states induce strong intensity fluctuations and adversely affect the PLE scans. The assumption that possibly very short T1 times may lead to a quick spin-repumping is unlikely, considering that Hahn echo measurements in a similar optical grade substrate show T2 times larger than 250 μs, which is in agreement with results demonstrated in Ref. [55]. Another possible interpretation could be that although we observe "permanently" bright lines, relatively fast ionization and reinitialization lead to compensation of spin-pumping-induced spin mixing under laser irradiation. Beyond the data shown in this work, time-resolved PLE data were investigated for specific on- and off-switching behavior. Despite sweeping the bin size from very short (revealing single-photon detection events) to timescales that would be visible in the PLE scans themselves, we were not able to identify these two regimes.

However, since the absence of spin mixing or benefits from unknown repumping mechanisms cannot be ruled out, spin-repump pulses are added to the entanglement generation protocol before every entanglement attempt. According to Humphreys *et al.* [11], we apply resonant repump pulses for the NV in a nanostructure equivalent to a power of 200 nW and a duration of 1.5 μs applied to NVs in bulk. In nanostructures with dimensions similar to the presented nanopillars and transferable to waveguide photonic crystal cavities, a field enhancement by a factor of about 15 is expected [35]. Therefore, we choose as spin-repump pulse parameters a power of 20 nW and a duration of 1 μs. The optical reset addresses both the $\mathrm{ms} = +1$ and -1 transitions. The spectral diffusion rate at 20 nW excitation, extracted from the fit presented in Fig. 3(c), is 55 MHz/s.

In Fig. 8, we show the performance of the protocol proposal with and without spin-repump pulses applied. Analogous to Fig. 5, we calculate the number of entanglement attempts that can be applied while spectral stability is maintained.

3. Ionization time

To get a rough estimate of the ionization time, we use the experimental data extracted from PLE measurements, presented in Fig. 2(c). Here, the NV ZPL transition is only driven when the laser is on resonance. However, most of the time during the PLE scans, the laser is off resonant. The duty cycle at which the ZPL transition is excited is about 0.2%. When π pulses of a duration of 2 ns and a power of 3.1 μW are applied at a repetition rate of 500 kHz, the resulting average excitation power is 3.1 nW. By multiplying the experimentally determined ionization time $t_{\mathrm{ion,PLE}} = 272.7$ s [Fig. 2(c)] at an excitation power of 3.1 nW with a duty cycle of 0.2%, a cw ionization time of $t_{\mathrm{ion,cw}} = 545.4$ ms results.

As a next step, we take additional spin-repump pulses into account. The ionization time is averaged over the whole entanglement generation sequence as labeled in Fig. 5(a). Here, the total ionization time depends on the inhomogeneous broadening criterion since, in the pulse sequence (including additional repump pulses) and spectral

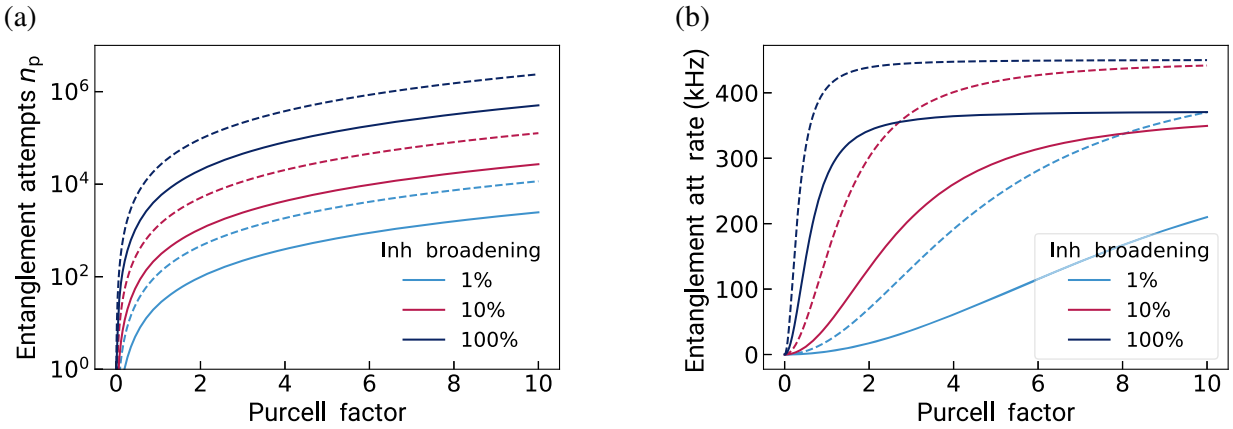

FIG. 8. Modified version of Fig. 5. We add to the proposal of entanglement generation (solid lines) the results of a modified protocol without considering resonant optical spin-repump pulses at 637 nm (20 nW, 1 μs) before every entanglement attempt (dashed lines).

realignment sequence (2 nW), different cw powers are applied. For example, for an inhomogeneous broadening criterion of 1% during entanglement attempts and subsequent performance of spectral realignment, the ionization time results in 558 ms.

APPENDIX E: ENTANGLEMENT PROTOCOL

We derive a quantitative estimate of the number of entanglement attempts (π-pulse excitations) given a certain spectral diffusion rate that can be applied until the linewidth is broadened by a certain amount. We base our estimates on the Wiener process, which provides an upper bound estimation for the inhomogeneous linewidth broadening and thus a lower bound on the number of attempts. The time-dependent FWHM of a Voigt profile, which broadens in time due to a random walk of the frequency, is given by

$$f_V(t) = a\sigma_{\mathrm{h}} + \sqrt{b\sigma_{\mathrm{h}}^2 + \sigma_{\mathrm{ih}}(t)^2}, \tag{E1}$$

where we used the approximation of the FWHM of a Voigt profile found in Ref. [56]. Note that σ_{hom} is the homogeneous linewidth, and the inhomogeneous contribution is linked to the spectral diffusion rate by

$$\sigma_{\mathrm{ih}}(t) = \Gamma_{\mathrm{SDR}}\sqrt{4\pi\ln(2)\tau t}, \tag{E2}$$

where τ is the time step for which Γ_{SDR} was determined and t is the time that has elapsed. The two constants are $a = 0.5346$, $b = 0.2166$. We can calculate the time it takes to broaden the line by p percent of its original value [$f_V(t_p) = (1+p)\sigma_{\mathrm{h}}$]:

$$t_p = \frac{(1+p-a)^2 - b}{4\pi\ln(2)\Gamma_{\mathrm{SDR}}^2\tau}\sigma_{\mathrm{h}}^2. \tag{E3}$$

The time t_p is determined by the spectral diffusion rate corresponding to the π-pulse power and the homogeneous linewidth of the emitter. We assume that between the π pulses, i.e., during darkness, spectral diffusion is not present. Hence, in a protocol based on single-shot excitation through π pulses with pulse duration T_π, the number of entanglement attempts during the time $t_{p,\pi}$ is given by

$$n_{p,\pi} = \frac{t_{p,\pi}}{T_\pi}. \tag{E4}$$

In a similar way, we calculate the broadening contribution from spin-repump pulses (Appendix D) before every entanglement attempt. Taking both contributions from π pulses and spin-repump pulses with different spectral diffusion rates and pulse durations into account, the number of entanglement attempts is given by

$$n_p = f\cdot n_{p,\pi} + (1-f)\cdot n_{p,\mathrm{spin-repump}}. \tag{E5}$$

The weighting factor f is determined by the condition for an equal number of π pulses and spin-repump pulses,

$$f\cdot n_{p,\pi} = (1-f)\cdot n_{p,\mathrm{spin-repump}}. \tag{E6}$$

The entanglement protocol consists of three parts, namely, NV initialization (charge-state preparation and spectral tuning), entanglement generation, and spectral realignment. Entanglement generation is achieved by applying resonant π pulses with interpulse delays of 2 μs (repetition rate of 500 kHz) to the system. During a heralded single-photon entanglement generation attempt, the spin state is prepared optically; a microwave pulse is used to create the superposition state; and finally, a resonant readout π pulse generates spin-photon entanglement followed by an additional microwave π pulse [11]. After the estimated time during which an inhomogeneous linewidth broadening of p percent is induced, a spectral realignment is performed. Here, the resonance is scanned in the vicinity (±10 MHz) of the target resonance frequency. The PLE scan is

performed at a scan speed of 6 GHz/s, resulting in a scan time of about 3.3 ms. Fitting the data and extracting the resonance center frequency would take less than 0.7 ms. Taking time for data processing and Stark tuning into account, we estimate a spectral realignment time of $t_{\mathrm{SpecCtrl}} = 5$ ms when no large spectral jumps occur. The number of entanglement attempts per ionization time (see Appendix D), where entanglement generation schemes and spectral realignment protocols are applied alternately, is calculated by

$$n_{\mathrm{ion}} = n_{p,\pi} \frac{t_{\mathrm{ion}}}{t_p + t_{\mathrm{SpecCtrl}}}. \tag{E7}$$

Here, t_p corresponds to the entanglement attempt number $n_{p,\pi}$ multiplied by the π pulse separation time of 2 μs.

When the NV ionizes, it would be reinitialized by a 5 μs green repump pulse and tuned again into resonance ($t_{\mathrm{init}} = 60$ ms). The high-energy initialization pulse likely causes a large spectral jump of the ZPL resonance within the inhomogeneous linewidth of 5 GHz. To localize the ZPL resonance after the initialization pulse, a PLE scan at a scan speed of 50 GHz/s is performed. On average, it takes 50 ms for the tunable laser to reach the resonance and induce an increase in count rate that will be detected. When the photon number passes a threshold significantly exceeding the dark count rate, the scan is stopped; the resonance would be localized and a dc voltage applied for tuning the ZPL resonance to the target frequency. For spectral fine-tuning, again, the spectral realignment scheme with PLE scans in the vicinity of the ZPL resonance frequency would be applied.

The final entanglement attempt rate is determined by normalizing the number of entanglement attempts during the ionization time by the total protocol duration

$$\Gamma_{\mathrm{EntAtt}} = \frac{n_{\mathrm{ion}}}{t_{\mathrm{ion}} + t_{\mathrm{init}}}. \tag{E8}$$

For increasing Purcell factors, a saturation of the entanglement attempt rate towards 370 kHz can be observed. The upper limit of the entanglement attempt rate is given by the repetition rate of 500 kHz as well as the ratio of entanglement generation time and system preparation time. Here, the shown entanglement attempt rate is not limited by physical laws but by technical issues that can be improved. For more details on the estimation of π-pulse parameters and the ionization time, the reader is referred to Appendix D.

APPENDIX F: STOCHASTIC DIFFUSION MODEL

We describe the spectral diffusion of the ZPL by a Wiener process, which can be modeled by the stochastic differential equation

$$\omega(t+\tau) = \omega(t) + \sigma Z\sqrt{\tau}, \tag{F1}$$

where Z is a normally distributed random variable (white noise) $p(Z) = \mathcal{N}(0,1)$ with mean $\mu = 0$ and variance $\sigma_z = 1$. The fixed time step τ corresponds to the time between repeated line scans in our experiments. We use this model for studying the time-dependent broadening of the spectral line as shown in Fig. 2(b). For the data sets that we studied, we did not find saturation of the inhomogeneous linewidth. Had the line stopped broadening, we would have done a more extensive analysis with the more appropriate Ornstein-Uhlenbeck process. The results that we obtained with the Ornstein-Uhlenbeck process (not shown) did not show better agreement with the experimental data.

The spectral diffusion rate we investigated in our experiments is given by

$$\Gamma_{\mathrm{SDR}} = \frac{\langle|\omega(t+\tau) - \omega(t)|\rangle}{\tau} = \frac{\sigma\langle|Z|\rangle}{\sqrt{\tau}}, \tag{F2}$$

which evaluates to

$$\Gamma_{\mathrm{SDR}} = \sigma\sqrt{\frac{2}{\pi\tau}}. \tag{F3}$$

We observe that the spectral diffusion rate scales like a square-root power law with respect to the intensity. We can thus connect the spectral diffusion rate to an intensity by assuming

$$\sigma = \sqrt{\eta(\omega_I,\tau)I}, \tag{F4}$$

where $\eta(\omega_I,\tau)$ is some proportionality constant that depends on the excitation frequency ω_I and the time step τ. Note that I is the intensity of the excitation light. We thus find, for the spectral diffusion rate,

$$\Gamma_{\mathrm{SDR}} = \sqrt{\frac{2I\eta(\omega_I,\tau)}{\pi\tau}}. \tag{F5}$$

From Eq. (F2), it follows that Γ_{SDR} is the average of the absolute value of the random variable,

$$Z_{\Gamma_{\mathrm{SDR}}} = \frac{\omega(t+\tau) - \omega(t)}{\tau}, \tag{F6}$$

which, by definition of the Wiener process (F1), is normally distributed:

$$p(Z_{\Gamma_{\mathrm{SDR}}}) = \mathcal{N}(0, \sigma/\sqrt{\tau}). \tag{F7}$$

When we compare the simulation and the experimentally measured distributions of Z_{SDR}, we find very good qualitative agreement (see, for example, Fig. 9). In Fig. 2(b), the results of using the Wiener process to find the inhomogeneously broadened linewidth can be seen. The goal is to find a distribution of inhomogeneous linewidths for 14 trajectories so that we can compare the simulated diffusion with the experimental results. For that purpose,

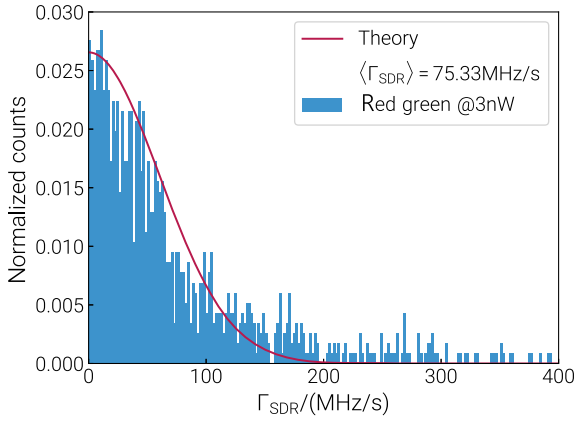

FIG. 9. Spectral diffusion rate distribution. Probability distribution of Γ_{SDR} for red and green excitation light at 5 nW. The distribution agrees well with the theoretical prediction (red) derived from the Wiener process at $\eta(\omega_I, \tau) = 3.41 \times 10^{24}/\mathrm{Joule/s^2}$ for a spectral diffusion rate of 75.35 MHz/s at 5 nW and $\tau = 2.3s$, which was used for modeling the diffusion process.

we numerically generate a large set of trajectories using Eq. (F1) with a spectral diffusion rate of $\Gamma_{\mathrm{SDR}} = 41$ MHz/s and a time step of 0.8 s. The set of trajectories is then divided into smaller sets of 14 lines. We use the following method to determine the distribution of inhomogeneous linewidths: At a given time step, the frequencies of 14 trajectories are taken as the center frequencies of 14 Lorentzians with a width of 60 MHz. This spectrum is then fitted with a Voigt profile, whose FWHM determines the inhomogeneous linewidth. We repeat this for all trajectory subsets and record their respective FWHMs. For each time step, we can then calculate the mean and the variance as shown in Fig. 2(b).

For smaller times, the selected trajectories do not fall within 1 standard deviation of the simulated linewidths. This can either be attributed to the postselection or subdiffusive behavior. For larger times, the mean of the simulated trajectories deviates significantly from the square-root behavior expected from a diffusion process. This can be attributed to using only very few spectral lines, which leads to large fluctuations in the fitting procedure.

We also use an Ornstein-Uhlenbeck process to model the diffusion of the spectral line. We did not find good qualitative agreement between the Ornstein-Uhlenbeck process and the broadening of the spectral line for various drift parameters. As discussed previously, the recorded trajectories did not have enough time to drift and thus to reproduce saturation of the inhomogeneous linewidth.

APPENDIX G: MONTE CARLO SIMULATION OF FLUCTUATING ELECTRIC FIELD

In this section, we detail our analysis of the contribution of a fluctuating charge environment to the inhomogeneously broadened ZPL of the NV center. The NV's ZPL is sensitive to local electric fields due to the lack of inversion symmetry. A fluctuating charge environment produces a fluctuating local electric field at the position of the NV, which, in turn, Stark shifts the position of the emission line. The accumulation of these shifts over time results in an inhomogeneously broadened spectral line. We investigated both the temporal change and the overall broadening in our experiments. The goal of this section is to make quantitative and qualitative estimates for the amount of broadening that is caused by a fixed number of charges in the NV's environment. Because we were able to observe trajectories of almost lifetime-limited spectral lines, we conclude that changes in the charge environment take place on timescales that are longer than the duration of individual line scans. We thus argue that a Monte Carlo simulation, in which we record the individual line shifts caused by randomly distributing a fixed number of charges in the NV's environment, is an adequate method to determine the line broadening produced by charge noise.

To tailor the Monte Carlo simulation as best as possible to the experimental conditions, we have to find the local electric field of a quasistatic charge distribution in a diamond nanopillar and determine the magnitude of the Stark shift. The tasks of finding the local field and its effect on the NV can be separated: In the following sections we present an expression for the electric field produced by the point charges inside a dielectric cylinder and a microscopic model of the interaction of a static field with the NV center. We then describe the details and the results of the Monte Carlo simulation. Charge screening is not systematically included in our simulations. However, screening charges would significantly dampen the electric field on length scales of the screening length and thus decrease the magnitude of field fluctuations at the location of the NV. This effect would lead to an overestimation of the SDR if the number of charges is kept fixed. When using the Thomas-Fermi model of screening, we find a screening length of a few nanometers, which would eliminate most of the SD. This means that a more involved model of screening is needed, which, given the excitation scheme, accurately predicts the trapped charge density and the delocalized charge density. The delocalized charges will then produce the screening effect. Such a model is beyond the scope of this paper, but it would be highly valuable. It would clarify how screening could be used to mitigate SD because screening reduces the impact of fluctuating charges on the NV's ZPL resonance.

1. Electric field of a charge in a dielectric cylinder

The goal of this section is to present closed expressions for the electric field produced by a group of point charges in a diamond nanopillar. This will allow us to efficiently determine the local electric field at the position of the NV. For this purpose, we approximate the nanopillar as a dielectric cylinder that has infinite length. This approximation will

hold as long as the Stark shifts that are produced by surface charges on the tip of the cylinder are smaller than the natural linewidth. The extension of the pillar into an infinite cylinder allows us to use the results of Ref. [57], where the electrostatic potential of a point charge in a cylindrical dielectric was calculated. According to Ref. [57], the potential of a point charge (in cylindrical coordinates) in a dielectric cylinder is

$$\phi(\mathbf{r},\mathbf{r}') = \frac{q}{4\pi^2\epsilon_0\epsilon_r}\int_0^\infty \mathrm{k}\cos[k(z-z')] \times \left[\frac{1}{2}I_0(k\rho_<)K_0(k\rho_>) + \sum_{m=1}^{\infty} I_m(k\rho_<)K_m(k\rho_>)\cos[m(\phi-\phi')]\right.$$
$$\left. - \frac{q_0(k)K_0(kR_0)}{2I_0(kR_0)}I_0(k\rho_<)I_0(k\rho_>) + \sum_{m=1}^{\infty}\frac{q_m(k)K_m(kR_0)}{I_m(kR_0)} \times I_m(k\rho_<)I_m(k\rho_>)\cos[m(\phi-\phi')]\right], \tag{G1}$$

where q is the charge, I_m and K_m are the modified Bessel functions, R_0 is the pillar's radius, $\rho_<$ and $\rho_>$ are the smaller and bigger radii when comparing the observation point $\mathbf{r}$ and the source point $\mathbf{r}'$,

$$q_m = \frac{1-\epsilon''/\epsilon'}{1-g_m(k)\epsilon''/\epsilon'}, \tag{G2}$$

where ϵ'' (ϵ') is the relative permittivity inside (outside) the pillar, and

$$g_m = \frac{K_m(kR_0)I'_m(kR_0)}{K'_m(kR_0)I_m(kR_0)}. \tag{G3}$$

The electric field is given by the gradient of the potential:

$$\mathbf{E}(\mathbf{r},\mathbf{r}') = -\nabla\phi(\mathbf{r},\mathbf{r}') \tag{G4}$$

$$= -\left(\boldsymbol{\rho}\partial_\rho\phi(\mathbf{r},\mathbf{r}') + \frac{1}{\rho}\boldsymbol{\varphi}\partial_\varphi\phi(\mathbf{r},\mathbf{r}') + \mathbf{z}\partial_{\mathbf{z}}\phi(\mathbf{r},\mathbf{r}')\right). \tag{G5}$$

For the Monte Carlo simulation, we assume that the NV is located on the symmetry axis of the cylinder. We can therefore place the coordinate origin at the location of the NV. The first two terms of the integrand in Eq. (G1) do not converge quickly. Fortunately, they can be evaluated [57] as the "direct" field of a charge, which is given by the potential

$$\phi'(\mathbf{r},\mathbf{r}') = \frac{q}{4\pi^2\epsilon_0\epsilon_r}\int_0^\infty \mathrm{k}\cos[k(z-z')]\left[\frac{1}{2}I_0(k\rho_<)K_0(k\rho_>) + \sum_{m=1}^{\infty} I_m(k\rho_<)K_m(k\rho_>)\cos[m(\phi-\phi')]\right]$$
$$= \frac{q}{4\pi\epsilon_0\epsilon_r}\frac{1}{\mathbf{r}-\mathbf{r}'}. \tag{G6}$$

If the observation point ($\mathbf{r}$) lies on the cylinder's axis, the derivation with respect to ϕ vanishes. The electric field at the origin thus becomes

$$\tilde{\mathbf{E}}(\mathbf{0},\mathbf{r}') = -\frac{q}{4\pi^2\epsilon_0\epsilon_r}(\mathbf{z}\partial_{\mathbf{z}} + \boldsymbol{\rho}\partial_\rho)\int_0^\infty \mathrm{k}\cos[k(z-z')]\frac{q_0(k)K_0(kR_0)}{2I_0(kR_0)}I_0(k\rho_<)I_0(k\rho_>)|_{\mathbf{r}=\mathbf{0}}, \tag{G7}$$

where $\mathbf{z}$ and $\boldsymbol{\rho}$ are unit vectors in the z and ρ directions so that

$$\mathbf{E}(\mathbf{0},\mathbf{r}') = -\nabla\phi'(\mathbf{r},\mathbf{r}')|_{\mathbf{r}=\mathbf{0}} + \tilde{\mathbf{E}}(\mathbf{0},\mathbf{r}'). \tag{G8}$$

The second term in the above equation can be interpreted as the effect of the surface polarization charge. For a group of charges, the field generated by multiple charges at the origin is given by

$$\mathbf{E} = \sum_{\mathbf{n}}\mathbf{E}(\mathbf{0},\mathbf{r}_\mathbf{n}) \tag{G9}$$

where $\mathbf{r}_n$ is the position of the $\mathbf{n}$th charge. The integral in Eq. (G7) is calculated numerically.

2. Interaction of NV with electric field

According to Ref. [58], the coupling of the electric field to the excited states is given by

$$H_E = g(b+d)E_z + gaM(\mathbf{E}), \tag{G10}$$

where

$$M(\mathbf{E}) = \begin{pmatrix} \mathbf{0} & \mathbf{0} & E_x - E_y\sigma_y \\ \mathbf{0} & E_x\sigma_z + E_y\sigma_x & \mathbf{0} \\ E_x - E_y\sigma_y & \mathbf{0} & \mathbf{0} \end{pmatrix}. \tag{G11}$$

Note that $\mathbf{E} = (\mathbf{E_x}, \mathbf{E_y}, \mathbf{E_z})$, σ_i are the Pauli matrices, and $\mathbf{0}$ is a two-by-two matrix with all entries equal to zero. Equation (G10) is stated in the basis $\{A_1, A_2, \tilde{E}_x, \tilde{E}_y, E_1, E_2\}$. We label the $\tilde{E}_x, \tilde{E}_y$, orbitals with a tilde to avoid confusion with the respective electric field components. The ground-state triplet couples to the electric field according to

$$H_E = 2gbE_z \tag{G12}$$

in the basis $\{^3A_{2+}, ^3A_{20}, ^3A_{2-}\}$. The coupling parameters are given by

$$g \approx 2 \text{ pHz}, \tag{G13}$$

$$a \approx b \approx c \approx 0.3\mu \text{ (MV/m)}^{-1}, \tag{G14}$$

$$d \approx 3\mu \text{ (MV/m)}^{-1}. \tag{G15}$$

To compare the Monte Carlo simulation with the experiment, we choose the $\tilde{E}_{x,y} \rightarrow {}^3A_{20}$ transition to determine the change of the transition energy due to the presence of an electric field. For this purpose, we diagonalize the above Hamiltonians for a given electric field and record the relative shifts in energy compared to the unperturbed energy of the $\tilde{E}_{x,y} \rightarrow {}^3A_{20}$ transition. The Stark shifts are given by

$$\Delta_\pm = (b-d)gE_z \pm ag\sqrt{E_x^2 + E_y^2}. \tag{G16}$$

The electric field lifts the degeneracy of the $\tilde{E}_{x,y}$ orbitals. In the experiments, we only resolve one spectral line. For the Monte Carlo simulations, we only use Δ_- because we assume that the other transition is not bright enough to be observed.

3. Results

a. Bulk

In this section, we present the results of the Monte Carlo simulation of the inhomogeneous linewidth produced by electric charges in the environment of the NV. For now, we do not consider any charge traps on the surface of the pillar and only focus on charges in the bulk. For the simulation, we randomly distribute charge traps in a cylindrical volume with the dimensions of the pillars used in the experiment ($r = 125$ nm, $h = 1600$ nm). We set the density of the charge traps to 1 ppm (approx. 13 800 traps) to imitate the density of the P1 centers, which we assume are the primary source of electric charge noise in our problem. P1 centers are likely to be electron donors, which makes them a likely candidate for a stationary charge impurity that can change its charge state during repeated line scans. A single iteration of our simulation consists of randomly distributing a fixed number of charges among the charge traps. The local electric field produced by the charges, which is calculated according to Eq. (G9), causes a change in the position of the resonance frequency as described by Eq. (G16). We assume global charge neutrality ($\sum_n q_n = 0$). After a fixed set of iterations, the frequency shifts are taken as the center frequencies of lifetime-limited Lorentzians. The resulting spectrum is the sum of all the Lorentzians. We fit the result

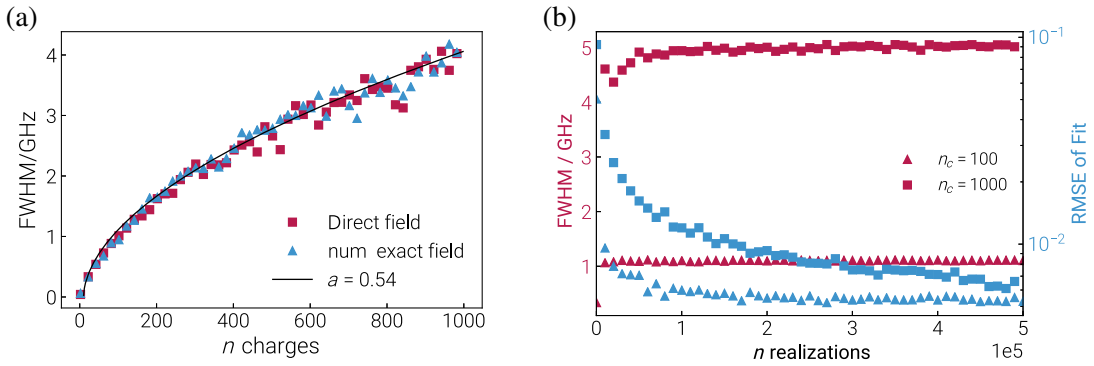

FIG. 10. Inhomogeneous broadening. (a) Inhomogeneous broadening caused by random distribution of charges with a density of 1 ppm (approx. 13800) in a cylindrical volume with a height of 1600 nm and a radius of 125 nm. The blue triangles are calculated using the electric field, including the contribution produced by the polarization surface charge [$\tilde{\mathbf{E}}$ in Eq. (G9)]. The red squares show the result of only including the direct field. The black line represents a fit with the power law $f(x) = b(x - x_0)^a$. (b) Blue triangles (100 charges) and squares (1000 charges) mark the FWHM of the inhomogeneous line for two different charge densities depending on the number of realizations of distributing the charges among the charge traps. The red squares and triangles show the root-mean-square error (RMSE) of the fit and the spectrum. The error drops for a higher count of realizations and appears to be saturating, indicating that the resulting spectrum reaches its equilibrium value. We chose 1000 realizations for the Monte Carlo simulation in panel (a).

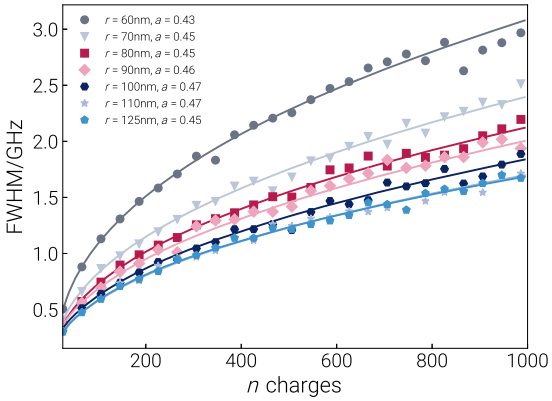

FIG. 11. Effect of surface charges on inhomogeneous linewidth. Inhomogeneous broadening due to surface charges for different pillar radii. The lines represent a fit with the power law $f(x) = b(x - x_0)^a$. The power law noticeably differs from the power law found for bulk charges [Fig. 10(a)].

with a Voigt profile to determine the linewidth of the inhomogeneously broadened line. The result of the procedure can be seen in Fig. 10(a). For the simulation 10 000 random charge distributions were sampled to produce a point in Fig. 10(a). The inhomogeneous linewidth shows reasonable saturation for 10 000 iterations [Fig. 10(b)]. In Fig. 10(a), no charge traps were placed on the surface of the cylinder. The surface charges are considered separately in the next section. The correction caused by surface polarization charges [$\tilde{\mathbf{E}}$ in Eq. (G9)] is almost negligible for the chosen geometry and the positioning of the NV center, as can be seen by comparing the squares and triangles in Fig. 10(a).

b. Surface

Here, we repeat the previous analysis, but we focus on surface defects. We apply the same reasoning as in the previous section but limit trap locations to the cylinder surface (6000 in total). Thus, we can make an estimate on the potential impact of surface charges and decide whether they are contributing to the field noise at the location of the NV. The impact of the trap density on the linewidth is no longer a big concern for larger densities. This can be seen, for example, in Fig. 14 where we investigated the inhomogeneous linewidth for different trap densities and a fixed amount of charge. The surface can have a significant impact on the broadening, as can be seen in Fig. 11, where the inhomogeneous broadening is shown for a range of different pillar radii. The impact of surface charges on the line broadening is more and more noticeable for smaller radii. It is interesting to observe that the power-law fits in Fig. 11 give exponents that are consistently below 0.5. This distinguishes a pure surface charge contribution to the broadening from randomly placing charges into the cylinder volume.

c. Surface vs bulk

In this section, we discuss the results of the impact on the line broadening of both fluctuating surface and bulk charges. Again, we assume a pillar with $h = 1600$ nm, $r = 125$ nm, and a NV that is located at its center. In each run of the simulation, a fixed amount of surface and bulk charges are allowed to assume random positions determined by fixed trap locations. The spectral diffusion rate is given by the difference of the Stark shifts of two subsequent charge configurations divided by a time step. Because the Monte Carlo simulation lacks any real time, an *ad hoc* time step has to be introduced such that the spectral diffusion rate and the broadening as predicted by the simulation match the experimental data for a fixed intensity. Here, we use the spectral diffusion rate of 1730 MHz/s and a total inhomogeneous broadening of 5 GHz. The inhomogeneous linewidth was measured by integrating over thousands of PLE scans at 37 nW excitation power and by applying strong green pulses between the PLE scans. The simulation

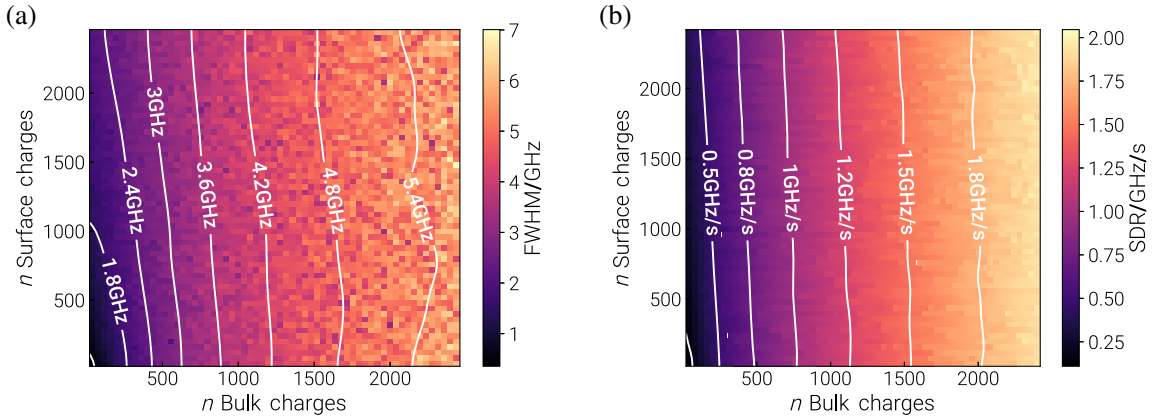

FIG. 12. Joint effect of surface and bulk charges. (a) Inhomogeneous broadening for a range of surface and bulk charges. (b) SDR calculated by fixing the time step per reordered charge configuration at 2000 bulk charges, which corresponds to a broadening of approximately 5 GHz (without screening).

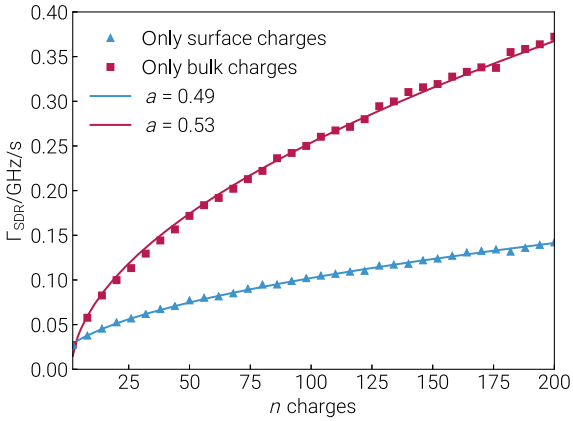

FIG. 13. Spectral diffusion rate scaling behavior. Shown are the SDR for no bulk charges (red triangles) and no surface charges (green squares) as a function of the number of charges contributing to the diffusion process. The parameters are the same as for Fig. 12. The solid lines correspond to a power-law fit with $\Gamma_{\mathrm{SDR}} = b(n - n_0)^a$. The power laws show a surprising similarity to the power laws in Fig. 3(c).

method could, in principle, allow us to predict the average amount of charge that contributes to the diffusion process by measuring the spectral diffusion rate. The results of the simulations can be seen in Figs. 12(a) and 12(b). We refrain from inferring real-world charge densities from comparing the Monte Carlo simulations with the experimental data. For a satisfactory comparison, charge screening has to be included in the simulation. Without screening, the Monte Carlo simulation underestimates the amount of charge contributing to the diffusion process. We could not determine the *ad hoc* time step for all excitation schemes because the linewidth did not always saturate [see, for example, Fig. 2(c)]. However, the qualitative behavior is not significantly impeded by these shortcomings of the simulation, and we see similarities in the scaling behavior of the SDR in the simulation and the experiment [compare Figs. 3(c) and 13].

d. Trap densities

In this section, we briefly comment on the relation between trap densities and the inhomogeneous line broadening. Performing the Monte Carlo simulations for different trap and charge densities revealed a negligible impact of the trap densities on the inhomogeneous linewidth. The same appears to hold for the spectral diffusion rate, which is given by the energy difference of two subsequent charge configurations divided by some arbitrary time step. The time step is not important here, as it does not impact the results. In Fig. 14, we show both the impact of changing the trap density on the line broadening and the spectral diffusion rate. Each point is averaged over ten trap densities equally spaced within 1 ppm increments. The error bars represent the standard deviation for both the linewidths and

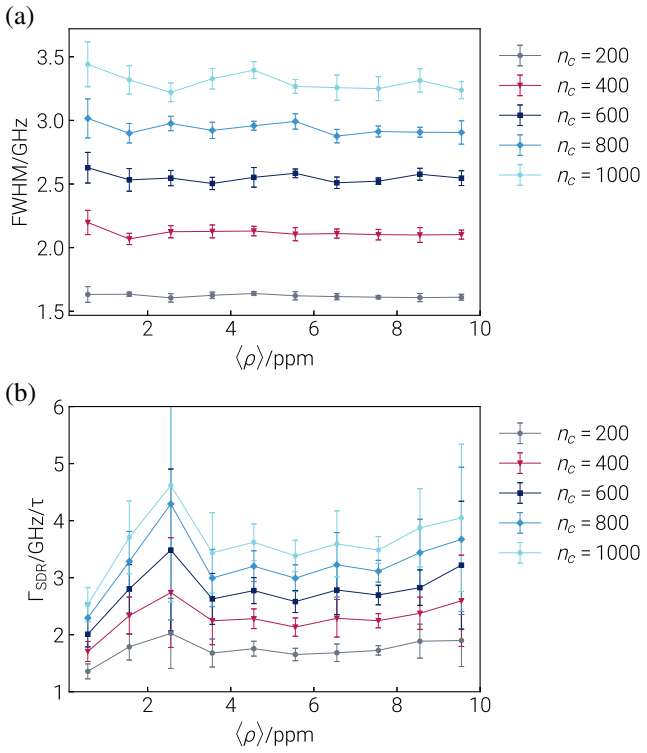

FIG. 14. Effect of trap densities. (a) Inhomogeneous linewidth and (b) spectral diffusion rate as a function of the trap density ρ/ppm for a range of charges and for 10 000 different configurations. Each point is averaged over ten trap densities equally spaced within 1-ppm increments. The error bars represent the standard deviation for both the linewidths and diffusion rates. The trap density appears to have little impact on the line broadening and the spectral diffusion range. The time step for the spectral diffusion rate is fixed to some arbitrary value, as it does not impact the qualitative behavior of the spectral diffusion rate.

diffusion rates. The result is somewhat surprising, as trap densities $\rho > 2$ ppm do not significantly decrease the spectral diffusion. The amount of charge that is free to fluctuate has a much greater impact for larger densities. A decrease in the spectral diffusion rate can be seen for densities $\rho < 2$ ppm. Here, a noticeable reduction in the rate of spectral jumps can be seen for smaller charge densities [see, e.g., the blue circles in Fig. 14(b), $n_c = 200$]. The spectral diffusion rate features some outliers, which are most likely an artifact of only considering a single trap configuration for each trap density.

[1] C. Degen, F. Reinhard, and P. Cappellaro, *Quantum Sensing*, Rev. Mod. Phys. **89**, 035002 (2017).
[2] F. B. Basset, M. Valeri, E. Roccia, V. Muredda, D. Poderini, J. Neuwirth, N. Spagnolo, M. B. Rota, G. Carvacho, F. Sciarrino, and R. Trotta, *Quantum Key Distribution with Entangled Photons Generated on Demand by a Quantum Dot*, Sci. Adv. **7**, eabe6379 (2021).

[3] A. Ekert and R. Renner, *The Ultimate Physical Limits of Privacy*, Nature (London) **507**, 443 (2014).
[4] M. Atatüre, D. Englund, N. Vamivakas, S.-Y. Lee, and J. Wrachtrup, *Material Platforms for Spin-Based Photonic Quantum Technologies*, Nat. Rev. Mater. **3**, 38 (2018).
[5] S. Wehner, D. Elkouss, and R. Hanson, *Quantum Internet: A Vision for the Road Ahead*, Science **362**, 303 (2018).
[6] H. J. Kimble, *The Quantum Internet*, Nature (London) **453**, 1023 (2008).
[7] J. Borregaard, H. Pichler, T. Schröder, M. D. Lukin, P. Lodahl, and A. S. Sørensen, *One-Way Quantum Repeater Based on Near-Deterministic Photon-Emitter Interfaces*, Phys. Rev. X **10**, 021071 (2020).
[8] P. Kok and S. D. Barrett, *Efficient High-Fidelity Quantum Computation Using Matter Qubits and Linear Optics*, Phys. Rev. A **71**, 060310(R) (2005).
[9] D. Englund, A. Faraon, I. Fushman, N. Stoltz, P. Petroff, and J. Vučković, *Controlling Cavity Reflectivity with a Single Quantum Dot*, Nature (London) **450**, 857 (2007).
[10] H. Bernien, B. Hensen, W. Pfaff, G. Koolstra, M. S. Blok, L. Robledo, T. H. Taminiau, M. Markham, D. J. Twitchen, L. Childress, and R. Hanson, *Heralded Entanglement between Solid-State Qubits Separated by Three Metres*, Nature (London) **497**, 86 (2013).
[11] P. C. Humphreys, N. Kalb, J. P. J. Morits, R. N. Schouten, R. F. L. Vermeulen, D. J. Twitchen, M. Markham, and R. Hanson, *Deterministic Delivery of Remote Entanglement on a Quantum Network*, Nature (London) **558**, 268 (2018).
[12] M. Pompili, S. L. N. Hermans, S. Baier, H. K. C. Beukers, P. C. Humphreys, R. N. Schouten, R. F. L. Vermeulen, M. J. Tiggelman, L. d. S. Martins, B. Dirkse, S. Wehner, and R. Hanson, *Realization of a Multinode Quantum Network of Remote Solid-State Qubits*, Science **372**, 259 (2021).
[13] J. P. Hadden, J. P. Harrison, A. C. Stanley-Clarke, L. Marseglia, Y.-L. D. Ho, B. R. Patton, J. L. O'Brien, and J. G. Rarity, *Strongly Enhanced Photon Collection from Diamond Defect Centers under Microfabricated Integrated Solid Immersion Lenses*, Appl. Phys. Lett. **97**, 241901 (2010).
[14] T. Schröder, S. L. Mouradian, J. Zheng, M. E. Trusheim, M. Walsh, E. H. Chen, L. Li, I. Bayn, and D. Englund, *Quantum Nanophotonics in Diamond [Invited]*, J. Opt. Soc. Am. B **33**, B65 (2016).
[15] N. H. Wan, B. J. Shields, D. Kim, S. Mouradian, B. Lienhard, M. Walsh, H. Bakhru, T. Schröder, and D. Englund, *Efficient Extraction of Light from a Nitrogen-Vacancy Center in a Diamond Parabolic Reflector*, Nano Lett. **18**, 2787 (2018).
[16] E. Neu, P. Appel, M. Ganzhorn, J. Miguel-Sánchez, M. Lesik, V. Mille, V. Jacques, A. Tallaire, J. Achard, and P. Maletinsky, *Photonic Nano-Structures on (111)-Oriented Diamond*, Appl. Phys. Lett. **104**, 153108 (2014).
[17] M. J. Burek, C. Meuwly, R. E. Evans, M. K. Bhaskar, A. Sipahigil, S. Meesala, B. Machielse, D. D. Sukachev, C. T. Nguyen, J. L. Pacheco, E. Bielejec, M. D. Lukin, and M. Lončar, *Fiber-Coupled Diamond Quantum Nanophotonic Interface*, Phys. Rev. Appl. **8**, 024026 (2017).
[18] C. G. Torun, P.-I. Schneider, M. Hammerschmidt, S. Burger, J. H. D. Munns, and T. Schröder, *Optimized Diamond Inverted Nanocones for Enhanced Color Center to Fiber Coupling*, Appl. Phys. Lett. **118**, 234002 (2021).
[19] L. Li, T. Schröder, E. H. Chen, M. Walsh, I. Bayn, J. Goldstein, O. Gaathon, M. E. Trusheim, M. Lu, J. Mower, M. Cotlet, M. L. Markham, D. J. Twitchen, and D. Englund, *Coherent Spin Control of a Nanocavity-Enhanced Qubit in Diamond*, Nat. Commun. **6**, 6173 (2015).
[20] S. L. Mouradian, T. Schröder, C. B. Poitras, L. Li, J. Goldstein, E. H. Chen, M. Walsh, J. Cardenas, M. L. Markham, D. J. Twitchen, M. Lipson, and D. Englund, *Scalable Integration of Long-Lived Quantum Memories into a Photonic Circuit*, Phys. Rev. X **5**, 031009 (2015).
[21] L. V. H. Rodgers, L. B. Hughes, M. Xie, P. C. Maurer, S. Kolkowitz, A. C. Bleszynski Jayich, and N. P. de Leon, *Materials Challenges for Quantum Technologies Based on Color Centers in Diamond*, MRS Bull. **46**, 623 (2021).
[22] A. Faraon, C. Santori, Z. Huang, V. M. Acosta, and R. G. Beausoleil, *Coupling of Nitrogen-Vacancy Centers to Photonic Crystal Cavities in Monocrystalline Diamond*, Phys. Rev. Lett. **109**, 033604 (2012).
[23] K.-M. C. Fu, C. Santori, P. E. Barclay, L. J. Rogers, N. B. Manson, and R. G. Beausoleil, *Observation of the Dynamic Jahn-Teller Effect in the Excited States of Nitrogen-Vacancy Centers in Diamond*, Phys. Rev. Lett. **103**, 256404 (2009).
[24] Y. Chu, N. de Leon, B. Shields, B. Hausmann, R. Evans, E. Togan, M. J. Burek, M. Markham, A. Stacey, A. Zibrov, A. Yacoby, D. Twitchen, M. Loncar, H. Park, P. Maletinsky, and M. Lukin, *Coherent Optical Transitions in Implanted Nitrogen Vacancy Centers*, Nano Lett. **14**, 1982 (2014).
[25] S. B. van Dam, M. Walsh, M. J. Degen, E. Bersin, S. L. Mouradian, A. Galiullin, M. Ruf, M. IJspeert, T. H. Taminiau, R. Hanson, and D. R. Englund, *Optical Coherence of Diamond Nitrogen-Vacancy Centers Formed by Ion Implantation and Annealing*, Phys. Rev. B **99**, 161203(R) (2019).
[26] M. Kasperczyk, J. A. Zuber, A. Barfuss, J. Kölbl, V. Yurgens, S. Flågan, T. Jakubczyk, B. Shields, R. J. Warburton, and P. Maletinsky, *Statistically Modeling Optical Linewidths of Nitrogen Vacancy Centers in Microstructures*, Phys. Rev. B **102**, 075312 (2020).
[27] S. Chakravarthi, C. Pederson, Z. Kazi, A. Ivanov, and K.-M. C. Fu, *Impact of Surface and Laser-Induced Noise on the Spectral Stability of Implanted Nitrogen-Vacancy Centers in Diamond*, Phys. Rev. B **104**, 085425 (2021).
[28] V. Yurgens, A. Corazza, J. A. Zuber, M. Gruet, M. Kasperczyk, B. J. Shields, R. J. Warburton, Y. Fontana, and P. Maletinsky, *Spectrally Stable Nitrogen-Vacancy Centers in Diamond Formed by Carbon Implantation into Thin Microstructures*, Appl. Phys. Lett. **121**, 234001 (2022).
[29] J. Wolters, N. Sadzak, A. W. Schell, T. Schröder, and O. Benson, *Measurement of the Ultrafast Spectral Diffusion of the Optical Transition of Nitrogen Vacancy Centers in Nano-Size Diamond Using Correlation Interferometry*, Phys. Rev. Lett. **110**, 027401 (2013).
[30] M. Ruf, M. IJspeert, S. van Dam, N. de Jong, H. van den Berg, G. Evers, and R. Hanson, *Optically Coherent Nitrogen-Vacancy Centers in Micrometer-Thin Etched Diamond Membranes*, Nano Lett. **19**, 3987 (2019).

[31] I. Lekavicius, T. Oo, and H. Wang, *Diamond Lamb Wave Spin-Mechanical Resonators with Optically Coherent Nitrogen Vacancy Centers*, J. Appl. Phys. **126**, 214301 (2019).

[32] S. Sangtawesin, B. L. Dwyer, S. Srinivasan, J. J. Allred, L. V. Rodgers, K. De Greve, A. Stacey, N. Dontschuk, K. M. O'Donnell, D. Hu, D. A. Evans, C. Jaye, D. A. Fischer, M. L. Markham, D. J. Twitchen, H. Park, M. D. Lukin, and N. P. de Leon, *Origins of Diamond Surface Noise Probed by Correlating Single-Spin Measurements with Surface Spectroscopy*, Phys. Rev. X **9**, 031052 (2019).

[33] H. Fotso, A. Feiguin, D. Awschalom, and V. Dobrovitski, *Suppressing Spectral Diffusion of Emitted Photons with Optical Pulses*, Phys. Rev. Lett. **116**, 033603 (2016).

[34] *Element Six Technologies Ltd. (UK): SC plate CVD* 3.0 × 3.0 mm*, 0.25 mm thick,* ⟨100⟩*, PL* (2020), https://e6cvd.com/eur/material/single-crystalline/sc-plate-cvd-3-0x3-0x0-25mm-100-pl.html.

[35] T. M. Babinec, B. J. M. Hausmann, M. Khan, Y. Zhang, J. R. Maze, P. R. Hemmer, and M. Lončar, *A Diamond Nanowire Single-Photon Source*, Nat. Nanotechnol. **5**, 195 (2010).

[36] R. Metzler, J.-H. Jeon, A. G. Cherstvy, and E. Barkai, *Anomalous Diffusion Models and Their Properties: Non-stationarity, Non-ergodicity, and Ageing at the Centenary of Single Particle Tracking*, Phys. Chem. Chem. Phys. **16**, 24128 (2014).

[37] N. Aslam, G. Waldherr, P. Neumann, F. Jelezko, and J. Wrachtrup, *Photo-Induced Ionization Dynamics of the Nitrogen Vacancy Defect in Diamond Investigated by Single-Shot Charge State Detection*, New J. Phys. **15**, 013064 (2013).

[38] P. Siyushev, H. Pinto, M. Vörös, A. Gali, F. Jelezko, and J. Wrachtrup, *Optically Controlled Switching of the Charge State of a Single Nitrogen-Vacancy Center in Diamond at Cryogenic Temperatures*, Phys. Rev. Lett. **110**, 167402 (2013).

[39] I. Kiflawi, A. T. Collins, K. Iakoubovskii, and D. Fisher, *Electron Irradiation and the Formation of Vacancy-Interstitial Pairs in Diamond*, J. Phys. Condens. Matter **19**, 046216 (2007).

[40] J. Rosa, M. Vaněček, M. Nesládek, and L. M. Stals, *Photoionization Cross-Section of Dominant Defects in CVD Diamond*, Diam. Relat. Mater. **8**, 721 (1999).

[41] A. T. Collins, A. H. Lettington, and J. W. Steeds, *The Optical and Electronic Properties of Semiconducting Diamond*, Phil. Trans. R. Soc. A **342**, 233 (1993).

[42] H. Kaupp, T. Hümmer, M. Mader, B. Schlederer, J. Benedikter, P. Häusser, H.-C. Chang, H. Fedder, T. W. Haensch, and D. Hunger, *Purcell-Enhanced Single-Photon Emission from Nitrogen-Vacancy Centers Coupled to a Tunable Microcavity*, Phys. Rev. Appl. **6**, 054010 (2016).

[43] J. Riedrich-Möller, L. Kipfstuhl, C. Hepp, E. Neu, C. Pauly, F. Mücklich, A. Baur, M. Wandt, S. Wolff, M. Fischer, S. Gsell, M. Schreck, and C. Becher, *One- and Two-Dimensional Photonic Crystal Microcavities in Single Crystal Diamond*, Nat. Nanotechnol. **7**, 69 (2012).

[44] B. Kambs and C. Becher, *Limitations on the Indistinguishability of Photons from Remote Solid State Sources*, New J. Phys. **20**, 115003 (2018).

[45] V. M. Acosta, C. Santori, A. Faraon, Z. Huang, K.-M. C. Fu, A. Stacey, D. A. Simpson, K. Ganesan, S. Tomljenovic-Hanic, A. D. Greentree, S. Prawer, and R. G. Beausoleil, *Dynamic Stabilization of the Optical Resonances of Single Nitrogen-Vacancy Centers in Diamond*, Phys. Rev. Lett. **108**, 206401 (2012).

[46] M. K. Bhaskar, R. Riedinger, B. Machielse, D. S. Levonian, C. T. Nguyen, E. N. Knall, H. Park, D. Englund, M. Lončar, D. D. Sukachev, and M. D. Lukin, *Experimental Demonstration of Memory-Enhanced Quantum Communication*, Nature (London) **580**, 60 (2020).

[47] https://github.com/Integrated-Quantum-Photonics-Group/pleasant and https://github.com/Integrated-Quantum-Photonics-Group/NV_spectral_diffusion.

[48] K. J. Brown, E. Chartier, E. M. Sweet, D. A. Hopper, and L. C. Bassett, *Cleaning Diamond Surfaces Using Boiling Acid Treatment in a Standard Laboratory Chemical Hood*, J. Chem. Health Saf. **26**, 40 (2019).

[49] H. A. Atikian, A. Eftekharian, A. Jafari Salim, M. J. Burek, J. T. Choy, A. Hamed Majedi, and M. Lončar, *Superconducting Nanowire Single Photon Detector on Diamond*, Appl. Phys. Lett. **104**, 122602 (2014).

[50] J. M. Binder, A. Stark, N. Tomek, J. Scheuer, F. Frank, K. D. Jahnke, C. Müller, S. Schmitt, M. H. Metsch, T. Unden, T. Gehring, A. Huck, U. L. Andersen, L. J. Rogers, and F. Jelezko, *Qudi: A Modular Python Suite for Experiment Control and Data Processing*, SoftwareX **6**, 85 (2017).

[51] M. Newville, T. Stensitzki, D. B. Allen, and A. Ingargiola, *LMFIT: Non-Linear Least-Square Minimization and Curve-Fitting for Python (0.8.0)*, Zenodo (2014), 10.5281/zenodo.11813.

[52] J. Hartung, *Statistical Meta-Analysis with Applications* (Wiley, Hoboken, NJ, 2008).

[53] Y. Avni, *Energy Spectra of X-Ray Clusters of Galaxies*, Astrophys. J. **210**, 642 (1976).

[54] C. Cohen-Tannoudji, J. Dupont-Roc, and G. Grynberg, *Atom-Photon Interactions*, 1st ed. (Wiley-VCH, Berlin, 1998), ISBN 978-0-471-29336-1, https://www.wiley-vch.de/de/fachgebiete/naturwissenschaften/atom-photon-interactions-978-0-471-29336-1.

[55] E. Bauch, S. Singh, J. Lee, C. A. Hart, J. M. Schloss, M. J. Turner, J. F. Barry, L. M. Pham, N. Bar-Gill, S. F. Yelin, and R. L. Walsworth, *Decoherence of Ensembles of Nitrogen-Vacancy Centers in Diamond*, Phys. Rev. B **102**, 134210 (2020).

[56] J. J. Olivero and R. L. Longbothum, *Empirical Fits to the Voigt Line Width: A Brief Review*, J. Quant. Spectrosc. Radiat. Transfer **17**, 233 (1977).

[57] S. T. Cui, *Electrostatic Potential in Cylindrical Dielectric Media Using the Image Charge Method*, Mol. Phys. **104**, 2993 (2006).

[58] J. R. Maze, A. Gali, E. Togan, Y. Chu, A. Trifonov, E. Kaxiras, and M. D. Lukin, *Properties of Nitrogen-Vacancy Centers in Diamond: The Group Theoretic Approach*, New J. Phys. **13**, 025025 (2011).